actuators

MDPI

Article

Trajectory Tracking of Autonomous Excavator Based on RBF–PID–Admittance Hybrid Control

Tingting Wang, Xiaoyu Zhu, Faming Shao, Xiaohui He * and Yuzheng Zhu *

College of Field Engineering, Army Engineering University of PLA, Nanjing 210007, China; wangtingting@aeu.edu.cn (T.W.); zxylgd@163.com (X.Z.); shaofaming@aeu.edu.cn (F.S.)

* Correspondence: 19741018236@163.com (X.H.); zyzlgd2025@aeu.edu.cn (Y.Z.); Tel.: +86-150-0515-7588 (X.H.); +86-188-0126-0869 (Y.Z.)

Abstract

To enhance the tracking accuracy and compliance of unmanned excavators, a force–position heterogeneous dual-loop nested cooperative control strategy is proposed. The outer loop employs admittance control to establish a dynamic mapping between contact forces and position correction commands, converting abrupt force variations into compliant position compensation. The inner loop utilizes an RBF neural network for online gain scheduling of PID parameters, thereby suppressing residual tracking errors introduced by the outer loop. Furthermore, asymptotic stability of the heterogeneous dual-loop nested closed-loop system is demonstrated via the Lyapunov method. Simulation results indicate that, in terms of position control, the RMSE and MAE for all three joints remain within 1°, with steady-state tracking errors confined to ±2°; compared with conventional PID and RBF-PID controllers, the tracking accuracy is improved. Regarding force control, compliant regulation of excavation contact forces is achieved, thereby enhancing both the precision and robustness of trajectory tracking for unmanned excavators.

Keywords: autonomous excavator; trajectory tracking; RBF neural network; PID control; admittance control

1. Introduction

Hydraulic excavators [1,2] constitute the pivotal enabler for the intelligentization of construction machinery [3]. Unmanned operation technologies [4,5] facilitate autonomous execution of complex tasks such as trench excavation and slope finishing, among which trajectory tracking [6–8] represents a focal research domain. Nevertheless, the pronounced nonlinearities and time-varying parameters inherent to hydraulic systems, coupled with the severely uncertain contact forces between the bucket and soil/rock, render conventional fixed-parameter linear control strategies inadequate for high-precision trajectory tracking. Pure position control is prone to inducing actuator overload or system instability [9,10]. Consequently, the control system must possess force–position coordinated regulation capability [11] and integrate the complementary strengths of multiple strategies to simultaneously ensure accuracy, responsiveness, and environmental adaptability.

To address the aforementioned challenges, extensive research efforts have been conducted. Owing to its simple structure and ease of implementation, PID control has long served as the fundamental approach for excavator motion control [11]. Zhang et al. [12] established a two-degree-of-freedom dynamic model of the hydraulic excavator working mechanism and proposed a PID parameter-tuning method through experimental testing,

Check for updates

Academic Editor: Xiaozheng Jin

Received: 1 July 2026
Revised: 25 July 2026
Accepted: 27 July 2026
Published: 4 August 2026

Copyright: © 2026 by the authors. Licensee MDPI, Basel, Switzerland. This article is an open access article distributed under the terms and conditions of the Creative Commons Attribution (CC BY) license.

achieving effective trajectory tracking in a simulation environment. Liu et al. [13] employed an improved particle swarm optimization (IPSO) algorithm for adaptive tuning of PID gains, with co-simulation results demonstrating superiority over conventional PID in terms of stability, accuracy, and rapidity. Feng et al. [14] proposed a PID controller parameter optimization method based on an improved genetic algorithm (IGA), which exhibited enhanced trajectory tracking accuracy compared to the standard genetic algorithm (SGA)-tuned PID controller in horizontal straight-line and slope trajectory tracking experiments on an excavator. Nevertheless, the fixed gains of conventional PID controllers are incapable of adapting to drastic variations in operating conditions during excavation tasks, leading to significant degradation in tracking performance under load disturbances and parameter drift [15]. To mitigate this issue, radial basis function (RBF) neural networks have been extensively employed for adaptive tuning of PID parameters. Feng et al. [16] developed an adaptive sliding mode controller incorporating RBF neural-network compensation, which effectively suppressed chattering while preserving system robustness. Zhenmian et al. [17] proposed a compound control method combining RBF neural networks with conventional PID and applied it to the automatic trajectory control of single-bucket hydraulic excavators; simulation results indicated that the RBF neural network-based PID control outperformed conventional PID in control performance, with the additional capability of automatically adjusting control parameters to accommodate variations in operating conditions. Dong H Q et al. [18] integrated fast terminal sliding mode control, backstepping control, and fractional-order control, with experimental validation confirming the superiority of this compound strategy in precise tracking and vibration suppression. However, sliding mode-based control schemes remain inherently confined to single-loop or cascade control architectures, lacking explicit force–position coordination mechanisms. Concurrently, impedance and admittance control strategies have been adopted to achieve compliant interaction with the environment. Tafazoli et al. [19] proposed a position-based impedance control method and applied it to compliant motion control of a hydraulic excavator-type manipulator. Qin et al. [20] further developed an adaptive robust impedance control scheme incorporating energy-saving objectives, optimized for the excavator boom and arm systems. Dobson et al. [21] validated the effectiveness of admittance control in robotic loading operations through field experiments on an industrial-grade loader. Nevertheless, the inner loops of the aforementioned hybrid control schemes predominantly employ fixed-parameter PID or PD controllers, which suffer from limited tracking accuracy in the presence of strong nonlinearities [22–24], time-varying parameters, and unmodeled dynamics in hydraulic systems, thereby compromising the effectiveness of outer-loop force–position coordination. Furthermore, conventional hybrid position/force control necessitates mode switching between position control and force control, which tends to induce force impacts and trajectory oscillations during the switching transient, adversely affecting operational smoothness [25,26].

Table 1 presents a systematic comparative analysis of the proposed scheme against three categories of representative methods: RBF–PID control, admittance/impedance control, and sliding-mode/model predictive control. The comparison is conducted across five dimensions: control architecture, force–position coordination, inner-loop adaptivity, stability analysis, and principal limitations.

In summary, existing studies exhibit limitations at two levels: (1) the standalone RBF-PID scheme lacks an explicit force-control mechanism, rendering it incapable of accommodating abrupt variations in soil contact force; and (2) although existing hybrid control schemes have achieved force/position coordination, the adaptive capability of the inner loop remains insufficient, while mode switching introduces additional dynamic disturbances. To address these issues, a trajectory tracking method for unmanned excava-

tors based on RBF–PID–admittance compound control is proposed, enabling hierarchical decoupled treatment of environmental and system uncertainties. The admittance outer loop handles abrupt soil contact force variations, whereas the RBF-PID inner loop provides online compensation for hydraulic system nonlinearities and parameter drift. The main contributions are as follows:

(1) A compound control architecture is constructed by nesting an outer-loop admittance planner with an inner-loop RBF-PID adaptive tracker. The outer loop establishes a dynamic relationship between contact force and trajectory correction based on the admittance model, achieving compliant control during soil–machine interaction; the inner loop employs an RBF neural network for online PID parameter tuning, with control gains adaptively adjusted via gradient descent with a momentum term.

(2) Based on Lyapunov methods, it is proven that the admittance loop possesses input-to-state stability with respect to force/torque deviations, and that the projection-based RBF-PID controller achieves semi-global uniform ultimate boundedness. Furthermore, based on cascade system stability theory, semi-global uniform ultimate boundedness of the overall inner/outer-loop compound control system is established.

(3) Simulations under typical excavation conditions verify the significant advantages of the proposed control strategy in terms of trajectory tracking accuracy and compliance. At the position-control level, the root-mean-square errors of the three joints (boom, arm, and bucket) are constrained within 0.9674°, 0.6688°, and 0.7778°, respectively; the mean absolute errors are reduced to 0.6236°, 0.4903°, and 0.5714°, with steady-state tracking deviations strictly limited to within ±2°. Compared with PID and RBF-PID schemes, the proposed strategy demonstrates notable improvements in tracking accuracy. At the force-control level, the system achieves compliant regulation of excavation contact force.

Table 1. Comparison of the proposed scheme with the existing literature.

Comparison Aspect	RBF-PID Control	Admittance/Impedance Control	Sliding-Mode/Model Predictive Control	Proposed Scheme
Control Architecture	Single-loop	Dual-loop	Single-loop or cascade	Dual-loop
Force–Position Coordination	None	Continuous transition	Partial availability	Admittance-based continuous transition with RBF online tuning
Inner-Loop Adaptability	RBF-tuned PID	Fixed parameters	Model-dependent or sliding-surface dependent	RBF-based online adaptive PID parameterization
Stability Analysis	Single-loop proof	Ideal tracking assumed	Dependent on model fidelity	Proven in three-tiered hierarchy, subject to bounded trajectory assumption and RBF approximability of ideal PID gains
Primary Limitation	Lack of force control	Fixed inner-loop parameters, limited adaptability	Chattering/high computational complexity	Simplified soil model

The remainder of this paper is organized as follows. Section 2 presents the dynamic modeling and kinematic analysis of the autonomous hydraulic excavator, establishing a comprehensive multi-body mathematical framework encompassing electrohydraulic dynamics and soil–tool interaction mechanics. Section 3 delineates the proposed RBF–PID–admittance hybrid control methodology, wherein the outer-loop admittance regulator and inner-loop neural-adaptive compensator are systematically formulated; rigorous theoretical stability analysis utilizing Lyapunov-based techniques and cascade system theory

is subsequently conducted. Section 4 presents comparative numerical simulation campaigns to quantitatively validate the proposed control architecture, including performance benchmarking against conventional PID and standalone RBF-PID methodologies under representative excavation scenarios, alongside detailed analysis of force–position coordination characteristics. Finally, Section 5 concludes the paper with a synthesis of principal findings, acknowledges inherent limitations of the current investigation, and delineates prospective avenues for future research.

2. System Modeling and Analysis

2.1. Dynamics Model of Autonomous Excavator

The working device of the autonomous excavator is composed of the boom, the bucket rod, the bucket, the rotary device and the hydraulic drive system. As shown in Figure 1, the D-H coordinate system of the working device of the autonomous excavator is established. The fixed coordinate system is established on each joint connecting the rods in turn. The homogeneous transformation matrix is used to describe the relationship between the adjacent two-bar coordinate systems, and the position and posture of each joint of the working device are expressed as the relationship between different homogeneous matrices. The physical parameters of the working device and the D-H coordinate system are known to obtain the D-H parameter table and the joint parameters of the working device as shown in Table 2. The torsion angle α is the angle between the Z axes of two adjacent rods. The length a of the connecting rod is the minimum distance between the two adjacent Z axes. The joint variable θ is the angle between the two adjacent Z axes. The offset distance d of the connecting rod is the distance between the two common normals, which is equal to the distance between the two X axes [27,28].

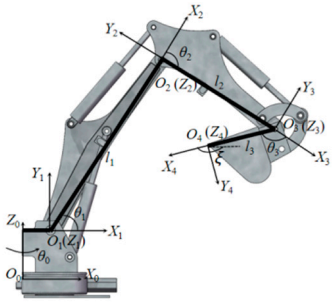


Figure 1. D-H coordinate system of autonomous excavator.

Table 2. D-H parameters of the working mechanism.

Joint i	θ_i	a_i	d_i	α_i
1	θ_1	a_0	d_0	$\frac{\pi}{2}$
2	θ_2	L_1	0	0
3	θ_3	L_2	0	0
4	θ_4	L_3	0	0

Dynamic analysis can solve the quantization problem of joint driving torque, inertia force and external load interaction, and provide the necessary dynamic constraints for the optimal design and energy consumption control of the motion system. Because the number of joints of the excavator working device is small, and the Lagrange method does not need to consider the internal stress of the rod in the calculation [29], the center of mass position of the rod is clear, and the distance, mass and running attitude can be solved dynamically. In summary, this paper uses the Lagrange method to establish the dynamic model of the working device, ignoring the influence factors such as the external load of the system. The

dynamic model accurately describes the force and torque relationship of the excavator working device in the motion process through the systematic equation including the inertial matrix, Coriolis force, centrifugal force and gravity term. The working device and slewing device of the autonomous excavator are usually operated independently. The four-degree-of-freedom dynamic model will introduce unnecessary complex nonlinear terms, which cannot improve the description accuracy of the main operation process. Therefore, it can be assumed that the rotation angle θ_1 is zero [30]. Define the angle $\theta = [\theta_2 \cdot, \theta_3 \cdot, \theta_4]^T$. The kinetic energy and potential energy of the excavator working device are substituted into the Lagrange equation, and the general expression of the excavator dynamic model is obtained.

$$\mathbf{M}_{jk}(q)\ddot{q} + \mathbf{C}_{jk}(q, \dot{q})\dot{q} + \mathbf{G}_j(q) = \tau_\omega \tag{1}$$

In the above formula, $q = [\theta_2, \theta_3, \theta_4]^{\mathrm{T}}$ is the joint variable vector; $\boldsymbol{M}_{\mathrm{jk}}$ is the positive-definite inertia matrix of the working device; $\boldsymbol{C}_{\mathrm{jk}}$ is the centrifugal force and Coriolis force matrix; $\boldsymbol{G}_{\mathrm{j}}$ is the gravity term; τ_ω is the control torque at the joint.

The matrix element $\boldsymbol{M}_{\mathrm{jk}}$ represents the coupling inertia between joint j and joint k, which is composed of the sum of the kinetic energy of all connecting rods:

$$M_{jk}(\mathbf{q}) = \sum_{i=1}^{3} \left[m_i \left(\mathbf{J}_{v_i}^{(j)} \right)^T \mathbf{J}_{v_i}^{(k)} + \left(\mathbf{J}_{\omega_i}^{(j)} \right)^T \mathbf{R}_i \mathbf{I}_i \mathbf{R}_i^T \mathbf{J}_{\omega_i}^{(k)} \right] \tag{2}$$

Among them, mi is the mass of each connecting rod;

$\mathbf{I}_i$ is the inertial tensor of each connecting rod around its centroid coordinate system;

$\mathbf{J}_{v_i}^{(j)}$ is the partial derivative of the centroid linear velocity of the connecting rod i to the generalized velocity $\dot{q}_j$;

$\mathbf{J}_{\omega_i}^{(j)}$ is the partial derivative of the angular velocity of the connecting rod i to the generalized velocity $\dot{q}_j$;

$\mathbf{R}_i$ is the rotation matrix from the coordinate system of the connecting rod i to the base coordinate system.

The matrix element $\boldsymbol{C}_{\mathrm{jk}}$ represents the Coriolis force and centrifugal force, which is composed of the product of the partial derivative of the inertial matrix and the joint velocity:

$$C_{jk}(\mathbf{q}, \dot{\mathbf{q}}) = \sum_{l=1}^{3} c_{jkl} \dot{q}_l \tag{3}$$

where the coefficient c_{jkl} is $c_{jkl} = \frac{1}{2}\left(\frac{\partial M_{jk}}{\partial q_l} + \frac{\partial M_{jl}}{\partial q_k} - \frac{\partial M_{kl}}{\partial q_j} \right)$.

The vector element G_j represents the equivalent torque generated by gravity on joint j, which is composed of the sum of the partial derivatives of the gravitational potential energy of each connecting rod to the generalized coordinates.

$$G_j(\mathbf{q}) = \sum_{i=1}^{3} m_i \mathbf{g}^T \mathbf{J}_{v_i}^{(j)} \tag{4}$$

where $\mathbf{g} = [0, 0, -g]^T$.

The dynamic model given by Equation (1) is formulated via the standard Lagrangian approach to establish the rigid-body dynamics of the excavator's working device, thereby furnishing a foundational dynamic framework for controller design. External loads, serving as environmental interaction forces, are characterized by the soil–bucket contact model presented in Section 2.3 and subsequently compensated as disturbance terms within the admittance control scheme elaborated in Section 3.2. Robustness of the system against bounded disturbances is guaranteed by the input-to-state stability (ISS) property.

The dynamics of the excavator working device system have the following characteristics [31]:

Property 1. *The inertial matrix M(q) is a positive-definite symmetric matrix. For any vector* $\theta \in \mathbf{R}^3$*, the following inequality is satisfied:*

$$\underline{\delta}\theta^{\tau}\theta \leq \mathbf{M}(q) \leq \overline{\delta}\theta^{\tau}\theta \tag{5}$$

Property 2. *The matrix* $\dot{\mathbf{M}}(q) - 2\mathbf{C}(q,\dot{q})$ *is skew-symmetric and satisfies for any nonzero vector* $\theta \in \mathbf{R}^3$*:*

$$\theta^T\left[\dot{\mathbf{M}}(q) - 2C(q,\dot{q})\right]\theta = 0 \tag{6}$$

Table 3 for the specific parameter values of the dynamic system. The detailed derivation of the dynamics matrix is provided in Appendix A.

Table 3. Parameters of dynamic system.

Parameter	Physical Quantity	Value	Unit
m_1, m_2, m_3	Masses of links	15, 9.8, 11.85	kg
I_{1z}, I_{2z}, I_{3z}	Moments of inertia	1.51, 0.56, 0.13	kg m^2
g	Gravitational acceleration	9.81	m/s^2
L_1, L_2, L_3	Distances between the joints	1.1, 0.83, 0.36	m

2.2. Hydraulic System Model

In the trajectory tracking control of hydraulic excavators, hydraulic system modeling is a necessary prerequisite to ensure control accuracy. When establishing the mathematical model of the hydraulic system of the hydraulic excavator working device, the following simplified assumptions are adopted: the hydraulic pump source is regarded as an ideal constant-pressure source, and the electromagnetic proportional valve is dynamically simplified as a static gain; it is assumed that the flow through the valve port is turbulent, and the volume elastic modulus of hydraulic oil is constant. Oil friction loss, oil mass and pipeline dynamic effects are ignored [32]. In addition, the complex soil load is simplified as a known torque acting on the joint. The displacement y of the hydraulic cylinder is obtained by the rope sensor. Two pressure sensors are also installed on the hydraulic system to measure the in-cylinder pressures p_1 and p_2 respectively. The oil supply pressure p_s and the oil return pressure p_o are constant values and zero values, respectively.

The asymmetric valve-controlled hydraulic cylinder is modeled, and the schematic diagram is shown in Figure 2:

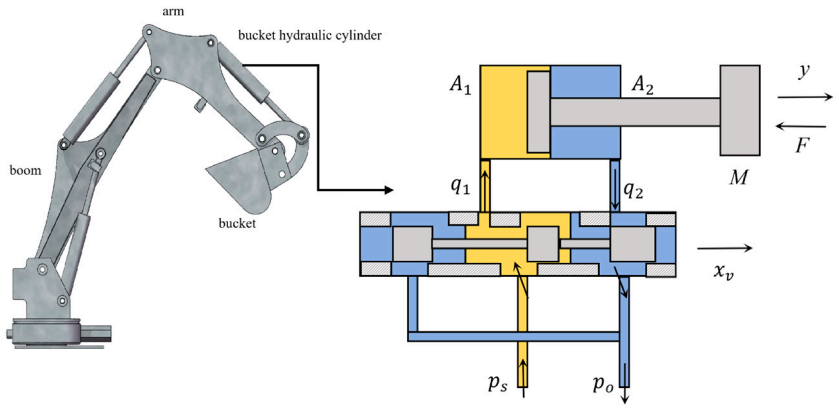


Figure 2. Structure diagram of valve-controlled hydraulic cylinder system.

Equation (7) describes the flow equation between the spool displacement and the load flow, and establishes the nonlinear relationship between the spool displacement and

the flow of the two chambers of the hydraulic cylinder. An equation describing the flow characteristics of a nonlinear main valve [33]:

$$Q_{\mathrm{L}} = Q_1 = C_{\mathrm{d}} w x_{\mathrm{v}} \sqrt{\frac{2}{\rho}\left(\frac{p_{\mathrm{s}} - p_L}{1+n^3}\right)} \tag{7}$$

$$\begin{cases} p_{\mathrm{L}} = p_1 - n p_2 \\ n = \frac{A_1}{A_2} \end{cases} \tag{8}$$

where C_d is the flow coefficient, w is the valve port area gradient, ρ is the oil density, P_s is the oil supply pressure, P_l is the load pressure, A_1 is the head-side area, A_2 is the rod-side area, and x_v is the piston displacement of the main valve.

The continuity equation takes into account the compressibility of the oil, the volume change in the cavity and the internal and external leakage, which is the key to connecting the flow and pressure dynamics. The continuity equation is established to describe the flow balance and pressure dynamics of the two chambers of the hydraulic cylinder.

$$Q_L = A_1 \dot{y} + \frac{V}{2(1+n^2)\beta_{\mathrm{e}}} \dot{p}_L + \frac{1+n}{1+n^2} C_{\mathrm{i}} p_L + \frac{1}{1+n^2} C_{\mathrm{o}} p_L \tag{9}$$

where y is the displacement of the hydraulic cylinder, C_i is the internal leakage coefficient, C_o is the external leakage coefficient, V and β_e are the total volume and effective bulk modulus of the chamber.

The force balance equation serves as the interface coupling the hydraulic and mechanical subsystems, bridging the hydraulic actuation force generated by the differential pressure across the two chambers with the inertial, damping, and excavation resistive forces acting on the piston and load.

$$A_1 P_1 - A_2 P_2 = m_t \ddot{y} + F_L \tag{10}$$

$$F_a = A_1 p_1 - A_2 p_2 = A_1 p_L \tag{11}$$

Among them, m_t is the equivalent mass of the piston, and the load F_L is the external load force acting on the piston, and F_a is the driving force of the hydraulic cylinder.

In the hydraulic excavator system, the response speed of the main valve is much higher than that of other hydraulic systems; ignoring the main valve dynamics, and simplifying the control input voltage u is proportional to the position of the valve core [34].

$$x_{\mathrm{v}} = K_{\mathrm{z}} u \tag{12}$$

where K_z is the amplification factor, and u is the input voltage.

According to Formulas (7)–(12), the relationship between the driving force and the control input can be calculated:

$$\dot{F}_a = A_1 \dot{p}_L = \frac{2A_1(1+n^2)\beta_{\mathrm{e}}}{V} \left(C_d w K_z u \sqrt{\frac{2}{r}\left(\frac{p_s - p_L}{1+n^3}\right)} - A_1 \dot{y} - \frac{1+n}{1+n^2} C_i p_L - \frac{1}{1+n^2} C_o p_L \right) \tag{13}$$

Ignoring hydraulic leakage, (13) can be expressed as:

$$\dot{F}_{\mathrm{a}} = A_1 \dot{p}_{\mathrm{L}} = \frac{2A_1(1+n^2)\beta_{\mathrm{e}}}{V} \left(C_{\mathrm{d}} w K_{\mathrm{z}} u \sqrt{\frac{2}{\rho}\left(\frac{p_{\mathrm{s}} - p_{\mathrm{L}}}{1+n^3}\right)} - A_1 \dot{y} \right) \tag{14}$$

2.3. Bucket–Soil Interaction Model

In order to realize the real-time correction of the trajectory of the bucket when it encounters excessive resistance to avoid structural damage, it is necessary to establish an interactive model that can characterize the dynamic mapping relationship between

the excavation resistance and the bucket motion. Therefore, this paper uses admittance control to adjust the desired trajectory according to the environmental interaction force [35]. Therefore, the model must meet two key requirements: first, it can reflect the current soil resistance characteristics in real time and provide a trigger basis for trajectory correction; second, the structure is simple, and the parameters can be updated online to adapt to changes in soil compactness or sudden obstacles. Considering that it is difficult to directly measure the pure cutting resistance of the soil to the bucket in actual operation, this paper takes the displacement of the bucket tip relative to the starting position as the input, and the digging resistance as the system output, and abstracts the impedance of the soil to the bucket as a time-varying second-order dynamic system. Considering that soil cutting involves complex shear failure, particle recombination and friction energy dissipation [36], it is difficult to meet the real-time control requirements if the fine discrete element model based on soil mechanics is used to calculate the complexity. Therefore, the complex stress field in the bucket–soil contact domain is equivalent to the dynamic relationship between measurable macro variables by using the lumped-parameter method [37,38]. The equivalent model includes equivalent mass, stiffness coefficient and damping coefficient [39,40]. This method not only retains the nonlinear mapping relationship between mining resistance and mining depth, but also ensures that the model structure is simple and the parameters can be updated online through real-time observation data.

The interaction between the hydraulic excavator attachment and the environment is set as the controlled object and modeled. As shown in Figure 3, the hydraulic excavator attachment is usually composed of three-link mechanisms, including the boom, the arm and the bucket, and the excavation operation is completed by linking each link mechanism. In some cases, the digging operation will also be carried out in coordination with the rotary motion of the hydraulic excavator body. In this study, only the mining process caused by the attachment operation is considered. The interaction between the excavator and the environment during the excavation process is local. The relationship between the excavation distance $y(t)$ and the excavation resistance $F_s(t)$ is assumed to be a system of resistance generated by mass, spring and damping elements [41]. The interaction model is shown in Figure 3 and expressed by the following continuous-time motion equation:

$$m\ddot{y}(t) + c\dot{y}(t) + k_{sp}y(t) = F_s(t) \tag{15}$$

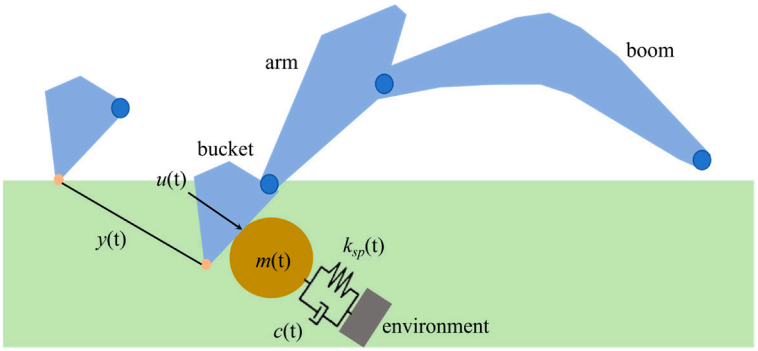


Figure 3. Environmental interaction model of autonomous excavator.

In the above formula, $y(t)$ is the excavation distance, $\dot{y}(t)$ and $\ddot{y}(t)$ are the velocity and acceleration respectively; $F_s(t)$ is the excavation resistance; m is the equivalent mass, representing the quality of the bucket and the soil being moved; c is the damping coefficient, which simulates the viscous resistance of soil and other media; k is the stiffness coefficient, which simulates the elastic restoring force of soil and other media.

It is difficult to use the sensor to detect the above parameters, so the above parameters are estimated. The mass m represents the equivalent mass of the soil and the bucket that is moved during the excavation process.

$$m = m_{bucket} + \lambda m_{soil} \tag{16}$$

In the above formula, m_{bucket} is the mass of the bucket, m_{soil} is the mass of the soil in the bucket, and λ is the proportional coefficient.

The quality of the soil in the bucket can be calculated by bucket capacity and soil density:

$$m = m_{bucket} + \lambda m_{soil} \tag{17}$$

In the above formula, V_{bucket} is the bucket capacity, and ρ_{soil} is the soil density.

Because the movement of the soil during the excavation process is not rigid, a proportional coefficient λ is introduced to be equivalent. λ represents the proportion of the soil quality that is actually driven by the bucket and produces inertial resistance in the total excavation soil quality in one excavation action. According to engineering experience, this paper sets λ to 0.5.

Therefore, the calculation formula of mass m is:

$$m \approx m_{bucket} + 0.5 \cdot V_{bucket} \cdot \rho_{soil} \tag{18}$$

In soil mechanics, the elastic modulus E of soil and the geometric characteristics of excavation can be used to estimate the excavation process. Assuming that the soil is similar to a spring in the excavation direction, its stiffness can be expressed as:

$$k_{sp} = \frac{EA}{L} \tag{19}$$

In the above formula, E is the elastic modulus of the soil, A is the effective area of the bucket in contact with soil, and L is the excavation depth. The selected soil parameters are presented in Table 4.

Table 4. Soil parameters.

Soil Type	Density kg/m^3	Young's Modulus (kPa)	Poisson Ratio	Moisture Content M (m^3·m^{-3})	Aggregation Force (kPa)
Clay soil	2500	3460	0.38	0.03	22.7

The c damping coefficient represents the damping characteristics of the soil, which is related to the internal friction and viscosity of the soil. It can be estimated from the damping ratio ζ of the soil. Most loam, wet sand and medium-hardness clay have both friction and certain viscosity. It is a common reference range in engineering. The soil damping ratio is selected as 0.4 in this paper.

According to the standard form of second-order systems:

$$\ddot{y} + 2\zeta\omega_n\dot{y} + \omega_n^2 y = \frac{u}{m} \tag{20}$$

where the natural frequency is $\omega_n = \sqrt{k_{sp}/m}$, and the damping ratio is ζ, known, then:

$$c = 2\zeta\sqrt{mk_{sp}} \tag{21}$$

According to Formulas (17) and (18), c can be estimated.

2.4. Establishment of State Space Equation

In order to facilitate the design of the subsequent controller, the nonlinear dynamic model of the excavator manipulator needs to be transformed into the form of a state space equation. The state space expression is not only beneficial to the stability analysis and control rate design of the control system, but also can intuitively describe the dynamic behavior of the system.

The state variable $\mathbf{x} = [q^{\mathrm{T}}, \dot{q}^{\mathrm{T}}, F_{\mathrm{a}}^{\mathrm{T}}]^{\mathrm{T}}$ is selected, where q is the joint angle, $\dot{q}$ is the joint speed, and F_a is the driving force of three hydraulic cylinders. To establish the state equation, it is necessary to clarify the mapping relationship between the physical quantities. The differential mapping between the piston displacement $y_{\mathrm{cyl}} = [y_1, y_2, y_3]^{\mathrm{T}}$ and the joint angle q of the hydraulic cylinder is defined as the hydraulic Jacobian matrix $J_{\mathrm{h}}(q)$.

$$\dot{y}_{\mathrm{cyl}} = J_{\mathrm{h}}(q)\dot{q} \tag{22}$$

The excavator working device model is expressed as the following state space form:

$$\dot{x}_1 = x_2 \tag{23}$$

$$\dot{x}_2 = M^{-1}(x_1)\left[J_{\mathrm{h}}^{\mathrm{T}}(x_1)x_3 - C(x_1, x_2)x_2 - G(x_1)\right] \tag{24}$$

$$\dot{x}_3 = \frac{2A_1(1+n^2)\beta_{\mathrm{e}}}{V}\left(C_{\mathrm{d}}wK_z u\sqrt{\frac{2}{\rho}\left(\frac{p_{\mathrm{s}} - x_3/A_1}{1+n^3}\right)} - A_1\dot{y}_{cy1}\right) \tag{25}$$

3. The Design of RBF–PID–Admittance Hybrid Controller

3.1. Overall Design of Controller

In the process of excavator operation, the contact characteristics between bucket and soil directly affect the operation quality and equipment safety. Although rigid position control can ensure trajectory accuracy, it is easy to produce excessive contact force and cause structural damage when encountering obstacles or resistance mutations. Simple force control is difficult to ensure the shape accuracy of the excavation trajectory. In order to achieve high-precision trajectory tracking control of autonomous excavators in complex environments and ensure the safety of operations when encountering sudden large resistance, this paper proposes an RBF–PID–admittance hybrid controller. The control block diagram is shown in Figure 4. The controller adopts a hierarchical architecture design, which combines trajectory tracking control with environmental interaction control. The outer-loop admittance controller corrects the desired trajectory in real time according to the interaction force between the bucket and the soil. The inner-loop RBF-PID controller uses the adaptive ability of the neural network to adjust the PID parameters online to ensure the accurate tracking of the modified trajectory. During the operation, the outer-loop admittance controller establishes a continuous mapping relationship between the contact force and the trajectory correction based on the soil impedance dynamics model, and calculates the admittance correction in real time. When the bucket is in free space, or the contact force is small, the correction is close to zero, and the RBF-PID controller tracks the original reference trajectory neural network to adjust the PID parameters online to adapt to the load change. With the increase in soil resistance, the admittance control dynamically generates the trajectory correction command according to the force deviation, and the RBF-PID controller tracks the expected trajectory after superposition correction to realize the hybrid adjustment of force and position. The controller adopts a layered architecture, in which an outer-loop admittance controller and an inner-loop RBF-PID controller operate in coordination. The outer loop takes the joint torque deviation $(\tau_d - \tau_e)$ as its input, where τ_e is computed from the internal states of the hydraulic system model via the hydraulic

Jacobian matrix, and τ_e is obtained by mapping the desired contact force through the bucket-tip Jacobian matrix. Through the joint-space admittance relationship, the outer loop generates the corrected desired joint trajectories $q_d, \dot{q}_d, \ddot{q}_d$. The inner loop takes the position tracking error $e = q_d - q$ as its input, and the RBF neural network performs online tuning of the PID parameters to produce the torque command τ. This command is then mapped through the proportional valve gain to the control voltage that drives the hydraulic system model. Subsequently, the hydraulic cylinder driving force F_a is mapped via the hydraulic Jacobian matrix J_h to the joint torque τ_ω, which acts upon the actuator model to close the control loop.

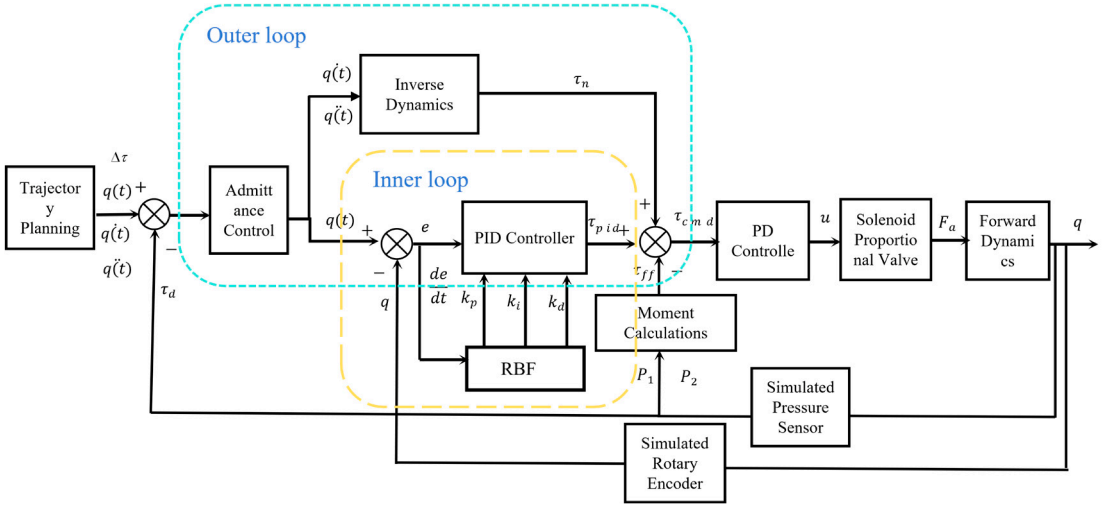


Figure 4. Block diagram of the RBF–PID–admittance hybrid control architecture.

3.2. Admittance Controller

In this paper, admittance control is introduced for trajectory tracking. By establishing the dynamic mapping relationship between contact force and motion correction, admittance control makes the excavator working device show the desired mechanical impedance characteristics in the process of interaction with soil, so as to avoid structural damage and maintain stable excavation efficiency. In this paper, the complex impedance effect of soil on the bucket is simplified as a lumped-parameter model. The model takes the displacement of the bucket tip relative to the starting position as the key variable, but no longer extends it to an independent state dimension. Instead, it is used as an internal calculation variable of the admittance controller to generate trajectory correction instructions [42,43]. Based on the bucket–soil interaction model established in Section 2.3, the admittance controller is devised within the simulation framework. In this simulation model, the pressures p_1 and p_2 within the dual chambers of the hydraulic cylinder are directly yielded by the hydraulic system model, thereby effectively emulating the pressure-sensing functionality of physical transducers employed in the actual hardware. The target dynamic equation of the admittance model is described as:

$$m_d(\ddot{\mathbf{q}}_d^{new} - \ddot{\mathbf{q}}_d^{ref}) + c_d(\dot{\mathbf{q}}_d^{new} - \dot{\mathbf{q}}_d^{ref}) + k_d(\mathbf{q}_d^{new} - \mathbf{q}_d^{ref}) = \mathbf{F}_a - \mathbf{F}_d \tag{26}$$

In the above formula, m_d is the expected inertia matrix, c_d is the expected damping matrix, k_d is the expected stiffness matrix, $\boldsymbol{F}_d$ is the expected contact force, and $\boldsymbol{F}_e$ represents the equivalent environmental contact force obtained from the actual measured contact force. This force is computed via the soil impedance dynamic model; $\mathbf{q}_d^{ref}$,$\dot{\mathbf{q}}_d^{ref}$,$\ddot{\mathbf{q}}_d^{ref}$ are the position, velocity and acceleration of the desired trajectory, respectively.

As this work is a simulation-based study, the system is not equipped with physical force sensors; consequently, Cartesian-space contact forces cannot be directly measured. In the simulation environment, the hydraulic system model provides the pressures p_1 and p_2 in the two chambers of the hydraulic cylinder, from which the driving force of the hydraulic cylinder is calculated using Equation (10). To enable joint-space control, the intrusion must be appropriately mapped. In order to realize joint-space control, it is necessary to map the intrusion displacement of Cartesian space to joint space. According to the hydraulic Jacobian matrix $J_{\mathrm{h}}(q)$ defined in Section 2.4 of Section 2, the relationship between the driving force of the hydraulic cylinder and the joint torque is:

$$J_{\mathrm{h}}(q) \tag{27}$$

Similarly, the small displacement of the bucket tip and the angular displacement of the joint satisfy:

$$\Delta y = J_{tip}\Delta q \tag{28}$$

In the above formula, J_{tip} is the Jacobian matrix of the bucket tip.

From Equation (28), the mapping from contact forces to joint torques is derived as $\tau_{em} = J_{tip}^{T}F_e$. Under the typical low-speed operating conditions of excavators, the hydraulic driving torques are essentially balanced by the environmental contact torques. Consequently, it is legitimate to substitute the environmental contact torque τ_{env} with the joint torque $\tau_e = J_h^T F_a$, which is computed from the hydraulic cylinder pressures as provided by the model. Accordingly, Equation (26) is converted into the joint space, yielding the joint-space admittance controller:

$$M_d^q(\ddot{q}_d - \ddot{q}_r) + C_d^q(\dot{q}_d - \dot{q}_r) + K_d^q(q_d - q_r) = \tau_e - \tau_d \tag{29}$$

In the above formula, $q_r, \dot{q}_r, \ddot{q}_r$ are the reference joint angle, angular velocity and angular acceleration of the trajectory planning input; $q_d, \dot{q}_d, \ddot{q}_d$ are the modified expected joint angle, angular velocity and angular acceleration output by the admittance controller; τ_d is the expected joint torque, derived from the desired contact force $\boldsymbol{F}_d$ via the bucket-tip Jacobian mapping. Concurrently, τ_e represents the simulated actual joint torque, which is computed from the cylinder pressures supplied by the hydraulic system model according to Equations (10) and (27). This computational process effectively emulates the pressure-sensing feedback functionality of physical transducers within the simulation environment.

In joint space, the admittance parameter matrices M_d^q, C_d^q, K_d^q prescribe the desired closed-loop dynamic characteristics to be realized by the controller. These matrices are tuned offline based on representative operating conditions and constitute inherent controller parameters, as opposed to physical parameters of the plant or the environmental medium. In this study, a diagonal positive-definite configuration is adopted, which remains constant throughout the control process: $M_d^q = \mathrm{diag}(m_{d,1}, m_{d,2}, m_{d,3})$, $C_d^q = \mathrm{diag}(c_{d,1}, c_{d,2}, c_{d,3})$, $K_d^q = \mathrm{diag}(k_{d,1}, k_{d,2}, k_{d,3})$. The diagonal entries are determined according to the soil–bucket interaction model elaborated in Section 2.3, along with the system dynamic response requirements. Specifically, $m_{d,3}$, corresponding to the bucket joint, incorporates the equivalent mass of the bucket and the soil to preclude abrupt jumps in acceleration commands, whereas $m_{d,1}$ and $m_{d,2}$, corresponding to the boom and arm joints, respectively, are set in accordance with the inertias of the respective links. The damping coefficients $c_{d,i}$ are tuned based on the soil damping ratio and the desired response speed to suppress oscillations during the correction transients, while the stiffness coefficients $k_{d,i}$ are referenced to the order of magnitude of the soil elastic modulus E to yield appropriate position corrections under abrupt resistance variations. The above parameters serve as nominal values under typical operating conditions and are intended to shape the desired closed-loop dynamic

behavior of the controller. Meanwhile, specific variations in soil properties affect only the magnitude of the torque deviation $\triangle\tau$, and the input-to-state stability (ISS) property guarantees system robustness against bounded disturbances.

3.3. RBF-PID Controller

The RBF-PID controller is used as the inner loop of the composite architecture to achieve spatial trajectory tracking. The radial basis function neural network is used to solve the shortcomings of PID control, such as strong nonlinearity and time-varying parameters of the excavator, with its local approximation characteristics and fast convergence ability. The controller can optimize the control gain online according to the running state of the system, and realize the coordinated improvement of tracking performance and robustness.

For each joint of the excavator working device, the traditional PID control law is:

$$u_i(t) = K_{p,i}e_i(q) + K_{i,i}\int_0^t e_i(q)d\tau + K_{d,i}\frac{de_i(q)}{dt} \tag{30}$$

In the above formula, i= 1, 2, 3 corresponds to the boom, arm and bucket joints, respectively, $K_{p,i}$, $K_{i,i}$ and $K_{d,i}$ are proportional, integral and differential gains, respectively.

RBF neural network adopts a three-layer feedforward structure: input layer, hidden layer and output layer.

Local input when each joint is independently adjusted:

$$\mathbf{x}_{in,i} = [e_i, \dot{e}_i, \Delta e_i]^T \tag{31}$$

In the above formula, $\Delta e_i = e_i(k) - e_i(k-1)$ is the error change rate, and $\dot{e}_i$ is the error differential signal.

The hidden layer uses the Gaussian radial basis function as the activation function. The output of the jth hidden layer neuron is:

$$h_j(\mathbf{x}) = \exp\left(-\frac{\|\mathbf{x} - \mathbf{c}_j\|^2}{2b_j^2}\right),\ j = 1, 2, \ldots, m \tag{32}$$

In the above formula, c_j is the center vector of the jth hidden layer neuron, b_j> 0 is the base width parameter of the jth hidden layer neuron, m is the number of hidden layer neurons, $\|\cdot\|$ represents the Euclidean norm.

The network output is three parameters of PID:

$$K'_{p,i} = \sum_{j=1}^{m} w_{pj}^{(i)} h_j(\mathbf{x}_{in}) \tag{33}$$

$$K'_{i,i} = \sum_{j=1}^{m} w_{ij}^{(i)} h_j(\mathbf{x}_{in}) \tag{34}$$

$$K'_{d,i} = \sum_{j=1}^{m} w_{dj}^{(i)} h_j(\mathbf{x}_{in}) \tag{35}$$

In the above formula, $w_{pj}^{(i)}, w_{ij}^{(i)}, w_{dj}^{(i)}$ is the output layer weight corresponding to the i th joint.

The above three parameters are normalized:

$$K_{p,i} = K_{p0,i} + \Delta K_{p,max,i} \cdot \text{sigmoid}(K'_{p,i}) \tag{36}$$

$$K_{i,i} = K_{i0,i} + \Delta K_{i,max,i} \cdot \text{sigmoid}(K'_{i,i}) \tag{37}$$

$$K_{d,i} = K_{d0,i} + \Delta K_{d,max,i} \cdot \text{sigmoid}(K'_{d,i}) \tag{38}$$

$$\text{sigmoid}(x) = \frac{1}{1+e^{-x}} \tag{39}$$

In the above formula, $K_{p0,i}$, $K_{i0,i}$, $K_{d0,i}$ are the initial setting values of PID parameters, $\Delta K_{p,max,i}$, $\Delta K_{i,max,i}$, $\Delta K_{d,max,i}$ are the boom limits of the parameter adjustment range, $\text{sigmoid}(\cdot)$ is the S-type activation function, and the network output is mapped to the [0, 1] interval to ensure that the parameters change smoothly within the preset safety range.

The RBF neural network optimizes the PID parameters by adjusting the weight of the output layer online. The gradient descent method is used to design the adaptive update law of the output layer weight of the RBF network, and the performance index function is defined as the square sum of the tracking error:

$$J_i = \frac{1}{2}e_i^2(k) \tag{40}$$

According to the gradient descent method, the weight correction should be along the negative gradient direction of J_i to the weight:

$$\Delta w_{pj}^{(i)}(k) = -\eta_p \frac{\partial J_i(k)}{\partial w_{pj}^{(i)}(k)} \tag{41}$$

where $\eta_p > 0$ is the learning rate. Using the chain rule to expand the partial derivative:

$$\frac{\partial J_i}{\partial w_{pj}^{(i)}} = \frac{\partial J_i}{\partial e_i} \cdot \frac{\partial e_i}{\partial q_i} \cdot \frac{\partial q_i}{\partial u_i} \cdot \frac{\partial u_i}{\partial K_{p,i}} \cdot \frac{\partial K'_{p,i}}{\partial K'_{p,i}} \cdot \frac{\partial K'_{p,i}}{\partial w_{pj}^{(i)}} \tag{42}$$

After derivation, the proportional channel weight update law is:

$$\Delta w_{pj}^{(i)}(k) = \eta'_p \cdot e_i(k) \cdot e_i(k) \cdot h_j(\mathbf{x}_{in}) \cdot \text{sgn}\left(\frac{\partial q_i}{\partial u_i}\right) \tag{43}$$

Similarly, the integral and differential channel weight update laws are:

$$\Delta w_{ij}^{(i)}(k) = \eta'_i \cdot e_i(k) \cdot \sum_{l=0}^{k} e_i(l) \cdot h_j(\mathbf{x}_{in}) \cdot \text{sgn}\left(\frac{\partial q_i}{\partial u_i}\right) \tag{44}$$

$$\Delta w_{dj}^{(i)}(k) = \eta'_d \cdot e_i(k) \cdot \Delta e_i(k) \cdot h_j(\mathbf{x}_{in}) \cdot \text{sgn}\left(\frac{\partial q_i}{\partial u_i}\right) \tag{45}$$

In order to accelerate convergence and suppress oscillation, the momentum term is introduced to obtain the final weight update formula:

$$\begin{aligned} w_{pj}^{(i)}(k) &= w_{pj}^{(i)}(k-1) + \Delta w_{pj}^{(i)}(k) + \alpha\left[w_{pj}^{(i)}(k-1) - w_{pj}^{(i)}(k-2)\right] \\ w_{ij}^{(i)}(k) &= w_{ij}^{(i)}(k-1) + \Delta w_{ij}^{(i)}(k) + \alpha\left[w_{ij}^{(i)}(k-1) - w_{ij}^{(i)}(k-2)\right] \\ w_{dj}^{(i)}(k) &= w_{dj}^{(i)}(k-1) + \Delta w_{dj}^{(i)}(k) + \alpha\left[w_{dj}^{(i)}(k-1) - w_{dj}^{(i)}(k-2)\right] \end{aligned} \tag{46}$$

In the above formula, $\alpha \in [0, 1)$ is the momentum factor, and its physical meaning is to retain the update trend of the previous moment, so that the weight adjustment has inertia and avoids violent oscillation at the steepness of the error surface.

The adaptive PID parameters are substituted into Formula (30) to obtain the control voltage of the ith joint:

$$u_i(k) = K_{p,i}e_i(k) + K_{i,i}\sum_{l=0}^{k} e_i(l) + K_{d,i}\Delta e_i(k) + u_{ff,i} \tag{47}$$

3.4. Stability Analysis of Compound Control

In this section, the theoretical stability of the RBF–PID–admittance hybrid controller is analyzed by constructing a Lyapunov function. The analysis is divided into three levels: first, the stability of the outer-loop admittance control is proved; second, the stability of the inner-loop RBF-PID control is proved; finally, the global stability of the composite control system is proved based on the cascade system theory.

3.4.1. Admittance Control Stability Analysis

The admittance controller is located in the outer loop of the composite control architecture, and its stability directly affects the effectiveness of trajectory correction and the security of the system. According to the dynamic equation of joint-space admittance control described by Equation (29), it constitutes the controller design equation. The parameters M_d^q, C_d^q, K_d^q are chosen as diagonal positive-definite matrices, with their values determined according to the soil model parameters detailed in Section 2.3 and the specified system dynamic response characteristics. The mechanical coupling among joints and the nonlinearities inherent in hydraulic actuation are lumped into the torque deviation term $\triangle\tau = \tau_e - \tau_d$. The trajectory deviation variable is defined:

$$\begin{aligned} e_a &= q_d - q_r \\ \dot{e}_a &= \dot{q}_d - \dot{q}_r \end{aligned} \tag{48}$$

The admittance kinetic equation can be written as:

$$M_d\ddot{e}_a + C_d\dot{e}_a + K_d e_a = \Delta\tau \tag{49}$$

In the above formula, $\triangle\tau = \tau_e - \tau_d$ is the torque deviation, as the input of the admittance system.

Provided that the desired admittance parameter matrices M_d^q, C_d^q, K_d^q are positive-definite diagonal and the torque deviation $\triangle\tau$ is bounded, the admittance control system is input-to-state stable (ISS), and the trajectory errors $e_a, \dot{e}_a$ are ultimately uniformly bounded.

The Lyapunov function is selected to prove:

$$V_a = \frac{1}{2}\dot{e}_a^T M_d \dot{e}_a + \frac{1}{2}e_a^T K_d e_a + \varepsilon e_a^T M_d \dot{e}_a \tag{50}$$

where ε is a small positive number, satisfying $\varepsilon < \min\left\{\frac{\lambda_{\min}(C_d)}{\lambda_{\max}(M_d)}, \sqrt{\frac{\lambda_{\min}(K_d)}{\lambda_{\max}(M_d)}}\right\}$ and ensuring that V_a is positive definite.

Derivation of V_a:

$$\dot{V}_a = \dot{e}_a^T M_d \ddot{e}_a + e_a^T K_d \dot{e}_a + \varepsilon \dot{e}_a^T M_d \dot{e}_a + \varepsilon e_a^T M_d \ddot{e}_a \tag{51}$$

We substitute the admittance kinetic equation into and sort out:

$$\dot{V}_a = -\dot{e}_a^T C_d \dot{e}_a + \dot{e}_a^T \Delta\tau + \varepsilon \dot{e}_a^T M_d \dot{e}_a - \varepsilon e_a^T C_d \dot{e}_a - \varepsilon e_a^T K_d e_a + \varepsilon e_a^T \Delta\tau \tag{52}$$

By using inequality scaling, there exists a positive number γ_1, γ_2 such that:

$$\dot{V}_a \le -\lambda_1 \|\dot{e}_a\|^2 - \lambda_2 \|e_a\|^2 + \gamma_1 \|\Delta\tau\|^2 \tag{53}$$

Among them, $\lambda_1 = \lambda_{\min}(C_d) - \varepsilon\lambda_{\max}(M_d) - \frac{1}{2}\gamma_2 > 0$, $\lambda_2 = \varepsilon\lambda_{\min}(K_d) - \frac{\varepsilon^2 \lambda_{\max}{}^2(C_d)}{2\gamma_2} > 0$.

Therefore, when $\|\Delta\tau\| \le \Delta_{\max}$, the admittance system satisfies the ISS property, and the trajectory deviation eventually converges to a bounded set: $\|e_a\| \le \sqrt{\frac{\gamma_1 \Delta_{\max}{}^2}{\lambda_2}}$, $\|\dot{e}_a\| \le \sqrt{\frac{\gamma_1 \Delta_{\max}{}^2}{\lambda_1}}$. The preceding ISS result establishes that, provided $\|\Delta\tau\| \le \Delta_{\max}$, the trajectory deviation converges asymptotically to a bounded set. The disturbance

upper bound $\triangle_{\max}$ is inherently determined by the soil resistance profile under varying operational scenarios. Specifically, during routine excavation where soil resistance remains within anticipated limits, $\triangle\tau$ is negligible, the admittance-loop correction tends to vanish, and the RBF-PID controller sustains high-fidelity tracking performance. Conversely, upon encountering obstacles or compacted strata, the increased $\triangle\tau$ invokes a trajectory correction e_a from the admittance loop, which is then promptly followed by the RBF-PID controller. Importantly, irrespective of soil property variations, the boundedness of $\triangle\tau$ ensures that constant admittance parameters are sufficient to guarantee the ISS of the closed-loop system. Although the diameter of the ultimate bounded set scales with $\triangle_{\max}$, the stability assertion itself remains invariant.

3.4.2. Stability Analysis of RBF-PID

As the inner loop tracking controller, the stability of the RBF-PID controller determines the tracking accuracy of the modified trajectory. In this paper, the single-joint extended tracking error, defined as $\boldsymbol{e}_i = \left[e_i, \int e_i\, dt, \dot{e}_i\right]^{\mathrm{T}} \in \mathbb{R}^3$ is employed as the state variable for continuous-time stability analysis. This state differs from the input to the RBF network in that the former incorporates the integral of the error, whereas the latter contains the rate of change in the error. In practical implementation, the integral term in Equation (47) is approximated by the discrete accumulation $\sum_{l=0}^{k} e_i(l)$ and the derivative term is approximated by $\Delta e_i(k) = e_i(k) - e_i(k-1)$. In the stability analysis, the closed-loop error dynamics are assumed to be expressible in the linearly parameterized form given by Equation (56), wherein the RBF network is utilized to adjust the PID gains online, thereby compensating for the severe nonlinearities and time-varying parameters inherent in the excavator dynamic model described in Section 2.

According to Section 3.3, the RBF-PID control law of the ith joint is: $u_i = k_p^i e_i + k_i^i \int e_i dt + k_d^i \dot{e}_i$.

Assumption 1. *There is an optimal weight vector W_i^*, so that the RBF network can accurately approximate the ideal PID parameters:*

$$k_j^{i*} = \sum_{l=1}^{m} w_{jl}^{i*} h_l(\mathbf{x}_i) + \epsilon_j^i,\ j \in \{p, i, d\} \tag{54}$$

The approximation error ϵ_j^i satisfies $\left|\epsilon_j^i\right| \leq \epsilon_M$, where ϵ_M is a small positive constant. We define the weight estimation error:

$$\widetilde{W}_i = W_i - W_i^* \tag{55}$$

where W_i is the actual weight vector.

Under the condition of satisfying Assumption 1, the RBF-PID control system is semi-globally uniformly ultimately bounded (SGUUB) by using the weight update law of Equation (46), and the tracking error and weight estimation error are uniformly ultimately bounded.

For the ith joint, the extended tracking error vector is defined as $\mathbf{e}_i = \left[e_i, \int e_i dt, \dot{e}_i\right]^T$, which is employed for continuous-time stability analysis. According to the dynamic model and hydraulic system model of the excavator in Section 2, the closed-loop error dynamics can be expressed as:

$$\dot{\mathbf{e}}_i = A_i \mathbf{e}_i + B_i(\widetilde{W}_i^T \mathbf{h}_i + \delta_i) \tag{56}$$

where A_i is the system matrix of appropriate dimensions, B_i is the input matrix, $\boldsymbol{h}_i = [h_1(\boldsymbol{x}_{\mathrm{in},i}), \cdots, h_m(\boldsymbol{x}_{\mathrm{in},i})]^{\mathrm{T}}$ denotes the output vector of the hidden layer of the RBF

network for the i-th, where m is the number of hidden-layer neurons. The weight estimation error matrix is defined as $\widetilde{W}_i = W_i - W_i^*$, with W_i^* being the ideal weight matrix, and δ_i represents the lumped disturbance term that encompasses neural-network approximation errors and unmodeled dynamics, satisfying $\|\delta_i\| \le \delta_M$. The rationale behind this linear parameterization lies in the following design: the RBF network outputs $K_{p,i}$, $K_{i,i}$, $K_{d,i}$ are normalized via a sigmoid function to yield bounded time-varying gains, i.e., $K_{p,i} \in \left[K_{p0,i},\ K_{p0,i} + \Delta K_{p,\max,i}\right]$, etc., such that the PID control law can compensate online for the inertial nonlinearities $M^{-1}(q)$, the centrifugal and Coriolis forces $C(q,\dot{q})\dot{q}$, the gravitational term $G(q)$, and the hydraulic actuation nonlinearities in the excavator dynamic model presented in Section 2. In actual implementation, Equation (47) is employed in discrete form, with the integral term approximated by $\sum_{l=0}^{k} e_i(l)$ and the derivative term approximated by $\triangle e_i(k)$.

Select the Lyapunov function:

$$V_p = \frac{1}{2}\mathbf{e}_i^T P_i \mathbf{e}_i + \frac{1}{2\eta}\mathrm{tr}(\widetilde{W}_i^T \widetilde{W}_i) \tag{57}$$

In Equation (57), P_i denotes a positive-definite symmetric matrix, which is determined by the Lyapunov equation $A_i^T P_i + P_i A_i = -Q_i$, where Q_i is a prescribed positive-definite symmetric matrix. This equation is employed to construct a Lyapunov function, and the existence of its positive-definite solution is ensured by the stability analysis presented subsequently. The parameter η represents the learning rate.

Derivation of V_p:

$$\dot{V}_p = -\frac{1}{2}\mathbf{e}_i^T Q_i \mathbf{e}_i + \mathbf{e}_i^T P_i B_i + \mathrm{tr}\left[\widetilde{W}_i^T\left(\mathbf{h}_i \mathbf{e}_i^T P_i B_i + \frac{1}{\eta}\dot{\widetilde{W}}_i\right)\right] \tag{58}$$

Using the standard gradient descent renewal law:

$$\dot{W}_i = -\eta \mathbf{h}_i \mathbf{e}_i^T P_i B_i - \alpha(W_i - W_i(t-T)) \tag{59}$$

where α is the momentum factor and T is the sampling period. When the momentum term is appropriately selected, the weight update guarantees: $\mathrm{tr}\left[\widetilde{W}_i^T\left(\mathbf{h}_i \mathbf{e}_i^T P_i B_i + \frac{1}{\eta}\dot{\widetilde{W}}_i\right)\right] \le 0$, therefore:

$$\dot{V}_p \le -\frac{1}{2}\lambda_{\min}(Q_i)\|\mathbf{e}_i\|^2 + \|\mathbf{e}_i\|\ \ \|P_i B_i\|\delta_M \tag{60}$$

When $\|\mathbf{e}_i\| > \frac{2\|PB_i\|\delta_M}{\lambda_{\min}(Q_i)}$, $\dot{V}_P < 0$, according to Lyapunov's stability theory, the tracking error is consistent and finally bounded.

To rigorously guarantee the boundedness of the weights, a modification term is incorporated into the boundedness analysis. When using $\sigma-$ correction, the update law is modified to:

$$\dot{W}_i = -\eta \mathbf{h}_i \mathbf{e}_i^T P_i B_i - \sigma W_i \tag{61}$$

where $\sigma > 0$ is a small constant, ensuring that the weight drift is bounded.

In the controller implementation, a momentum term is additionally incorporated to enhance convergence performance. The synergistic interplay of these two mechanisms is elaborated as follows. The momentum term, defined in Equation (46) with $\alpha \in [0,1)$, preserves the historical update direction and effectively dampens oscillatory behavior. Concurrently, the $\sigma-$ modification term, given in Equation (61) with $\sigma > 0$, serves to prevent weight drift. Under the proposed combined update law, the momentum term exerts no influence on the SGUUB boundedness result; it solely improves the transient convergence dynamics. In contrast, the σ-modification term rigorously ensures that $\mathrm{tr}\left[\widetilde{W}_i^{\mathrm{T}}\left(\mathbf{h}_i \mathbf{e}_i^{\mathrm{T}} P B_i + \frac{1}{\eta}\dot{\widetilde{W}}_i\right)\right] \le 0$.

Consequently, the Lyapunov derivative satisfies $\dot{V}_P \leq -\frac{1}{2}\lambda_{\min}(Q_i)\|\mathbf{e}_i\|^2 + \|\mathbf{e}_i\|\|PB_i\|\delta_M$, which implies that whenever $\|\mathbf{e}_i\| > \frac{2\|PB_i\|\delta_M}{\lambda_{\min}(Q_i)}$, the inequality $\dot{V}_P < 0$ holds, thereby guaranteeing uniform ultimate boundedness of the tracking error. To conclude, the weight update law for the RBF-PID controller is implemented and analyzed in a unified composite form: the momentum term accelerates convergence and suppresses oscillations, whereas the $\sigma-$ modification term ensures weight boundedness. These two terms are physically complementary rather than conflicting, and thus the SGUUB stability assertion holds rigorously.

3.4.3. Composite Control Stability Analysis

The composite control system is composed of a cascade of the outer ring admittance controller and the inner ring RBF-PID controller. The outer-loop admittance subsystem and the inner-loop RBF-PID subsystem are formulated in a cascade configuration as given by Equation (62) and Equation (63), respectively. The state-variable and input mappings are defined as follows. For the admittance loop, the state is $\boldsymbol{z}_1 = \left[e_a^T, \dot{e}_a^T\right]^{\mathrm{T}}$, with $e_a = q_d - q_r$ denoting the trajectory deviation, and the input is $\boldsymbol{u}_1 = \Delta\boldsymbol{\tau} = \boldsymbol{\tau}_e - \boldsymbol{\tau}_d$, which represents the torque deviation derived from the difference between the joint torque τ_e and the desired torque τ_d. For the RBF-PID loop, the state is $\boldsymbol{z}_2 = \left[\boldsymbol{e}^{\mathrm{T}}, \mathrm{vec}\left(\widetilde{W}\right)^{\mathrm{T}}\right]^{\mathrm{T}}$, where $\boldsymbol{e} = [e_1, e_2, e_3]^{\mathrm{T}}$ collects the tracking errors of the individual joints, and $\widetilde{W}$ denotes the weight error matrix of the RBF network. The input to this loop is $\boldsymbol{u}_2 = \left[q_d^{\mathrm{T}}, \dot{q}_d^{\mathrm{T}}, \ddot{q}_d^{\mathrm{T}}\right]^{\mathrm{T}}$, comprising the modified trajectory output from the admittance loop along with its first and second derivatives. The coupling between the two subsystems operates as follows: the admittance loop produces the modified trajectory q_d in response to the torque deviation $\Delta\tau$; this trajectory, after being mapped through the hydraulic Jacobian matrix $J_h(q)$, is used by the RBF-PID controller to generate the control voltage u, which in turn drives the hydraulic system to deliver the joint torque. Upon interaction with the soil, this torque yields a new $\Delta\tau$ that is fed back to the admittance loop, thereby closing the overall control loop.

We define the state $\boldsymbol{x} = \left[\mathbf{e}_a^{\mathrm{T}}, \mathbf{e}^{\mathrm{T}}, \mathrm{vec}\left(\widetilde{W}\right)^{\mathrm{T}}\right]^{\mathrm{T}}$ of the composite system, where $\boldsymbol{e}_a$ is the admittance trajectory deviation, $\boldsymbol{e}$ is the inner ring tracking error vector, and $\widetilde{W}$ is the RBF weight error matrix of all joints.

Assumption 2. *The modified trajectory $q_d(t)$ generated by the admittance controller and its derivatives $\dot{q}_d(t)$, $\ddot{q}_d(t)$ are uniformly bounded.*

The inner ring RBF-PID controller has finite-time convergence characteristics or exponential convergence characteristics.

The system satisfies the cascade structure: the admit ring output is used as the inner ring input, and the inner ring dynamically does not affect the admit ring in reverse.

Under the conditions of satisfying Hypotheses 1 and 2, the RBF–PID–admittance hybrid control system is semi-globally consistent and ultimately bounded. When the neural network approximates error $\epsilon_M \to 0$ and perturbs $\delta_M \to 0$, the system is close to stability.

The stability theory of a cascading system is used for analysis. Think of a composite system as a cascade of two subsystems:

For admitter rings are:

$$\dot{\mathbf{z}}_1 = f_1(\mathbf{z}_1, \mathbf{u}_1) \tag{62}$$

where $\mathbf{z}_1 = [e_a^T, \dot{e}_a^T]^T$, enter $\mathbf{u}_1 = \Delta\tau$. Section 3.4.1 analyzes that the subsystem satisfies the properties of the ISS, and the existence of the ISS Lyapunov function V_a and the $\mathcal{K}_\infty$-class function $\alpha_1, \alpha_2, \gamma_1$ makes that:

$$\begin{aligned} &\alpha_1(\|\mathbf{z}_1\|) \le V_a(\mathbf{z}_1) \le \alpha_2(\|\mathbf{z}_1\|) \\ &\dot{V}_a \le -\alpha_3(\|\mathbf{z}_1\|) + \gamma_1(\|\mathbf{u}_1\|) \end{aligned} \tag{63}$$

For RBF-PID rings are:

$$\dot{\mathbf{z}}_2 = f_2(\mathbf{z}_2, \mathbf{u}_2) \tag{64}$$

where $\mathbf{z}_2 = [\mathbf{e}^T, \mathrm{vec}(\widetilde{W})^T]^T$, enter $\mathbf{u}_2 = [q_d^T, \dot{q}_d^T, \ddot{q}_d^T]^T$. The subsystem is analyzed in Section 3.4.2 to meet the characteristics of the ISS.

The output of the admittance ring is used as the reference input of the RBF-PID ring, and the output of the RBF-PID ring is fed back to the admittance ring through pressure measurement to form a closed loop. Consider the compound Lyapunov function:

$$V_c = V_a + \mu V_p \tag{65}$$

where $\mu > 0$ is the weight coefficient.

For V_c, using the properties of the ISS and the Young inequality:

$$\dot{V}_c \le -[\alpha_3(\|\mathbf{z}_1\|) - \mu\gamma_2(\|\mathbf{z}_1\|)] - \mu\frac{\lambda_{\min}(Q)}{2}\|\mathbf{z}_2\|^2 + \gamma_1(\|\Delta\tau\|) \tag{66}$$

If you choose μ to be sufficiently small compared to $\alpha_3(\|\mathbf{z}_1\|) - \mu\gamma_2(\|\mathbf{z}_1\|) \ge \frac{1}{2}\alpha_3(\|\mathbf{z}_1\|)$, then:

$$\dot{V}_c \le -\frac{1}{2}\alpha_3(\|\mathbf{z}_1\|) - \mu\frac{\lambda_{\min}(Q)}{2}\|\mathbf{z}_2\|^2 + \gamma_1(\Delta_{\max}) \tag{67}$$

Therefore, when $\|z\| > \chi(\Delta_{\max})$, $\dot{V}_c < 0$, where χ it is a function of class κ. This proves the SGUUB stability of the composite system.

Ideally, when $\epsilon_M = 0$ and $\delta_M = 0$, the RBF-PID ring achieves asymptotic tracking, i.e., $\mathbf{e} \to 0$. At this time, the admittance ring input $\Delta\tau$ only contains the soil impedance deviation, and if the soil model is accurate, then $\Delta\tau \to 0$ and then $\mathbf{e}_a \to 0$. Therefore, the whole system is gradually stabilized.

In the actual excavation operation: the soil resistance is within the expected range, $\Delta\tau$ is small, the admittance ring correction is close to 0, $q_d \approx q_r$, and RBF-PID achieves high-precision trajectory tracking. When encountering obstacles or dense soil, the trajectory correction e_a is generated by increasing the admittance ring of $\Delta\tau$, and the RBF-PID quickly tracks the corrected trajectory to ensure the safety of the contact force. The corrected trajectory keeps the contact force within a safe range, and the system enters a new steady state, with all errors consistently bounded.

It is noteworthy that the validity of the aforementioned stability conclusions rests upon the following five standard premises, the underlying physical interpretations and limitations of which merit explicit clarification:

(1) The bounded-disturbance premise ($|\delta_i| \le \delta_M$) presumes that external disturbances possess finite energy. In the event of extreme scenarios such as rock jamming that induce abrupt resistance variations beyond the prescribed bound, the SGUUB conclusion may temporarily cease to hold.

(2) The bounded-approximation-error premise derives from the universal approximation capability of RBF neural networks on compact sets. Should the joint trajectory extend beyond the workspace covered by the distribution of RBF centers, the approximation error may potentially diverge.

(3) The ideal Jacobian-mapping premise assumes that the inverse dynamics of the hydraulic system are known exactly. Nevertheless, parametric uncertainties arising from factors such as viscosity–temperature variations in hydraulic fluid and wear of valve orifices are not explicitly incorporated into the stability analysis; instead, their robustness is indirectly compensated for by the online adaptive nature of the RBF network.

(4) Positive-definiteness premise of the relevant matrices is ensured via judicious design of the admittance and Lyapunov matrices. The selection of parameters inherently involves a trade-off between response rapidity and stability margin; excessively high-stiffness gains may render the system susceptible to high-frequency disturbances.

(5) The existence-of-optimal-RBF-weights premise treats the optimal weight W_i solely as a virtual reference for theoretical purposes. The stability result guarantees bounded convergence of the estimation error $\widetilde{W}_i$, but does not ensure convergence of W_i itself to the ideal value. The actual convergence precision is governed jointly by the learning rate, the persistence of excitation, and the architectural complexity of the network.

The limitations inherent in these premises imply that the current stability conclusions are conditional in nature. In practical deployment, they should be evaluated in conjunction with specific operating constraints and established parameter-tuning guidelines.

4. Simulation Analysis

4.1. Simulation Platform and Parameter Settings

The simulation platform in this paper is based on the MATLAB environment, which mainly includes the kinematics model of the excavator robotic arm, the hydraulic actuator model, the soil environment model, and the control system. The simulation model is shown in Figure 5. To reduce model complexity while focusing on the primary objective of control strategy validation, the hydraulic system simulation model employed in this study is subject to the following simplifying assumptions [44,45]: (1) the pump source is modeled as an ideal constant-pressure supply, with pressure ripple and pump dynamics neglected; (2) the proportional valve is approximated by a static gain model, neglecting spool dynamics, dead-zone, and saturation nonlinearities; (3) distributed-parameter characteristics of hydraulic pipelines and pressure-wave propagation effects are disregarded; and (4) both internal and external leakages of the hydraulic cylinders are omitted. These simplifications are justifiable during the simulation-based validation phase of the control strategy; nevertheless, they inevitably introduce certain modeling inaccuracies. Specifically, the constant-pressure assumption yields an overoptimistic estimate of supply pressure under substantial load variations; the static valve model fails to capture spool response delays under high-frequency operating conditions; and the neglect of leakage leads to an overestimation of positional accuracy during low-speed holding phases. Consequently, the simulation results presented herein primarily reflect the trajectory tracking performance of the control strategy under idealized hydraulic conditions, and their extrapolation to real-world excavation scenarios necessitates further verification through subsequent refined hydraulic modeling and physical experiments. The PID controller parameters are empirically tuned via the trial-and-error method, as summarized in Table 5. The initial parameters of the RBF-PID controller and the RBF–PID–admittance hybrid controller are consistent with those of the PID controller. The RBF neural network is configured with Gaussian basis functions and a hidden layer comprising six neurons, a choice that balances the input dimensionality against real-time computational limitations. The centers are uniformly positioned along each error axis within the normalized input space $[-1,1]^3$, taking the coordinate set $\{-1,-0.6,-0.2,0.2,0.6,1\}$. A basis function width of $\sigma = 0.5$ is selected to ensure adequate overlap between adjacent basis functions across the input space, thus preserving the continuity of local approximation. Online weight adaptation is

performed via gradient descent augmented with a momentum term, where the learning rate is set to $\eta = 0.1$ and the momentum coefficient to $\alpha = 0.05$. Furthermore, a projection mechanism is applied to confine the weights within the bounded interval $[-2,2]$, effectively preventing unbounded parameter drift. The output-layer weights are initialized to zero, placing the initial gains at the midpoint between the baseline PID parameters and the maximum adjustable gains. This ensures that the controller possesses an adaptive margin from the very beginning of operation and avoids the initial response lag that would arise from learning from scratch. The Cartesian space position correction limit of the admittance controller is plus or minus 10 cm, and the joint-space correction amplitude is plus or minus 10°. The simulation solver is set to a fixed step of 0.001 s for a total simulation of 60 s, and the ODE23T algorithm is adopted; the sampling period of the controller is synchronized with the simulation step to ensure real-time performance. The controller is synchronized with the simulation step to guarantee real-time performance. The simulation solver utilizes the ode23t variable-step stiff solver to address the stiffness inherent in the hydraulic–mechanical coupled system, with a maximum step size of 0.001 s imposed to ensure the discretization accuracy of the controller. The controller module operates in Simulink at a fixed sample time of 0.001 s, which is synchronized with the maximum step size of the solver, thereby ensuring both numerical stability and precise alignment of the control period. The per-cycle computational burden of the control algorithm primarily consists of the forward propagation of the RBF network and the Jacobian mapping for admittance control, both of which entail relatively low computational complexity. The control strategy is therefore theoretically feasible for real-time implementation; however, its practical performance is subject to hardware resources, operating system scheduling, and I/O latency, among other factors, which warrant further validation in subsequent physical experiments. The configuration parameters of the simulation platform and the control system are listed in Table 6.

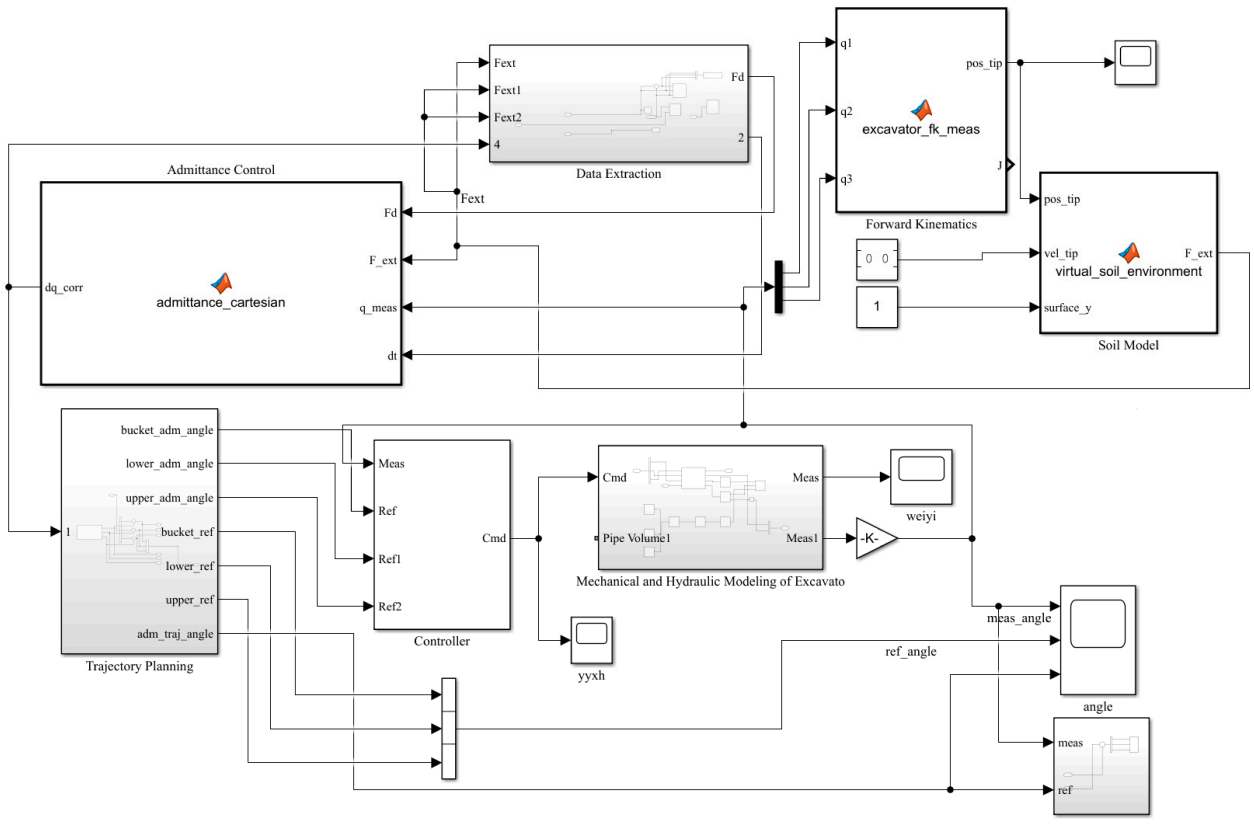


Figure 5. RBF–PID–admittance hybrid controller Simulink model.

Table 5. PID controller parameters.

Joint	Kp	Ki	Kd
Boom	30	0.5	0.1
Arm	24	0.3	0.06
Bucket	10	0.01	0.01

Table 6. Simulation platform and control system configuration parameters.

Category	Parameter	Setting
Simulation environment	Software platform	MATLAB R2020b/Simulink
	CPU	Intel Core i7-10700 @ 2.90 GHz
Solver settings	Solver type	ode23t
	Simulation duration	60 s
	Relative tolerance	1×10^{-3}
	Maximum step size	0.001 s

4.2. Trajectory Tracking Simulation of Different Controllers

In order to verify the effectiveness of the RBF–PID–admittance hybrid control strategy in a typical operation cycle, based on the timing of the excavation conditions defined in Table 7, three strategies of traditional PID control, RBF-PID adaptive control and RBF–PID–admittance hybrid control proposed in this paper are used to carry out three-joint trajectory tracking simulation experiments. The tracking accuracy of each controller is quantitatively evaluated by comparing the joint angle response characteristics of each controller under the same reference trajectory. The trajectory tracking time–domain response and steady-state error analysis results of the three controllers are shown in Figures 6–8.

Table 7. Excavation condition time series.

Phase	Temporal Interval	Operation Stage
I	0~10 s	Initial attitude adjustment
II	10~30 s	Dig into the cut
III	30~40 s	Full bucket ascension
IV	40~50 s	Unloading and locating
V	50~60 s	Unloading reset

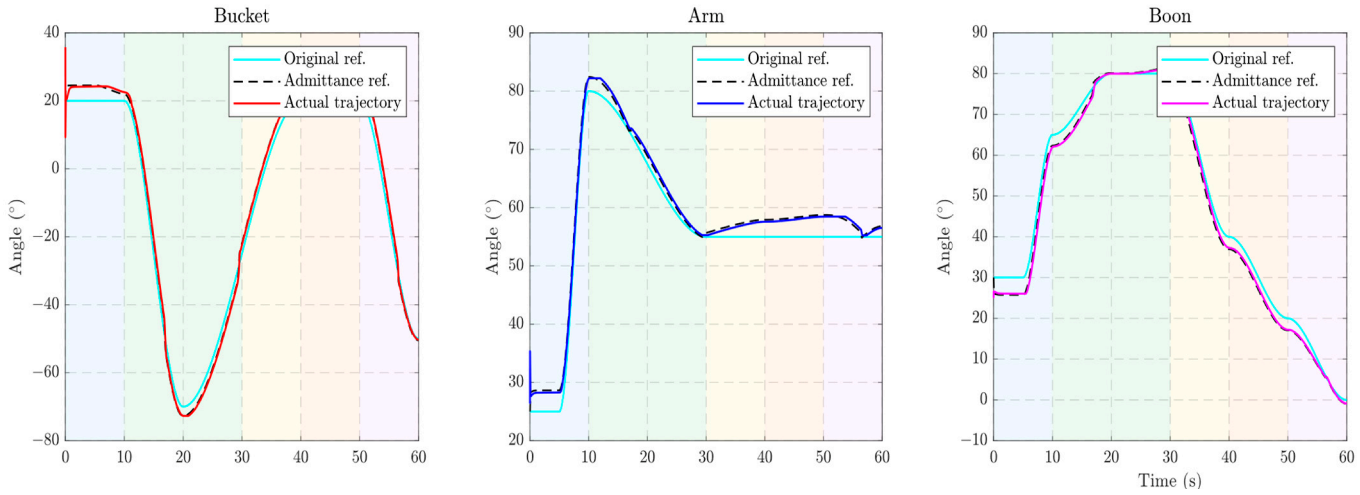


Figure 6. RBF–PID–admittance hybrid controller trajectory tracking.

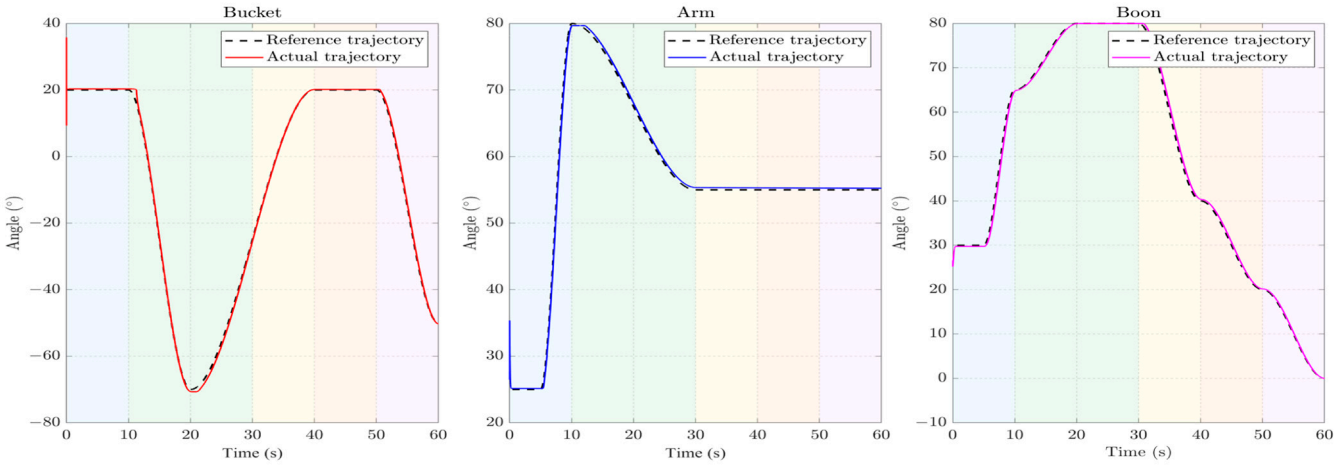


Figure 7. Trace tracking of RBF-PID controller.

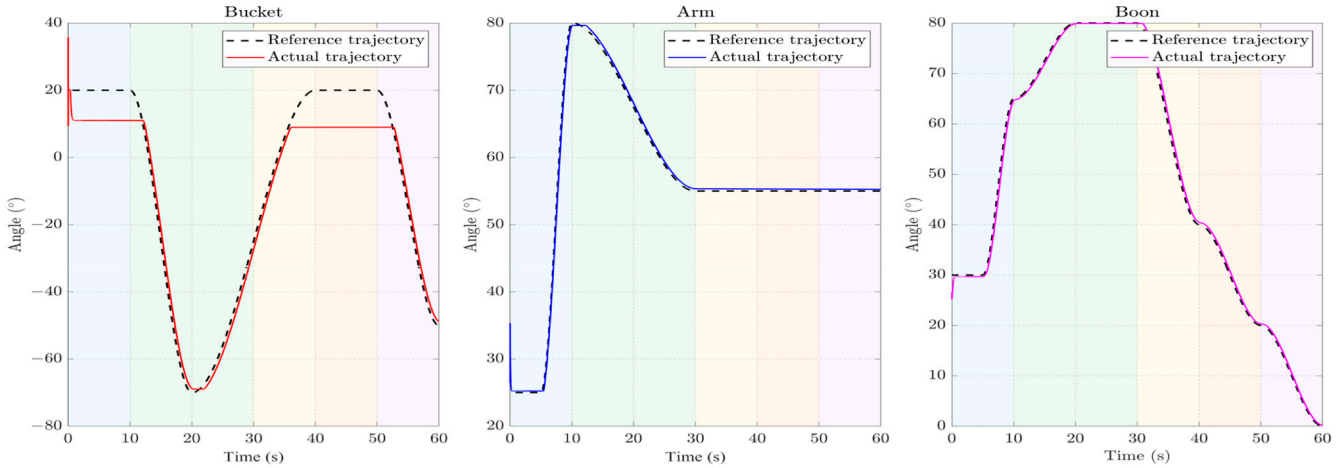


Figure 8. PID controller trajectory tracking.

The trajectory tracking time–domain response curve analyzes the positional servo performance of the three control strategies in the typical excavation cycle. The joint angle response of the traditional PID controller (as shown in Figure 6) shows obvious hysteresis characteristics during the initial attitude adjustment of stage I, and there is a large overshoot during the excavation and cutting process of stage II, and the actual trajectory deviates significantly from the reference trajectory. In contrast, the RBF-PID controller (shown in Figure 7) shows faster dynamic response and smaller tracking lag during stage III full bucket lifting and stage IV unloading positioning through the online learning ability of the neural network. After the introduction of the admittance control link, the trajectory fit of the RBF–PID–admittance hybrid controller (as shown in Figure 8) is significantly improved at each stage, especially in the process of stage V discharge and reset; its response curve almost coincides with the reference trajectory, indicating that the proposed strategy effectively suppresses the trajectory offset caused by external load disturbance while ensuring position accuracy. From the comparison of the three joints, the tracking difference between the three controllers is the most significant due to the large inertia and drastic load change in the bucket joint. However, due to the relatively small range of motion of the Boom joint, the tracking curves of each controller are relatively close, but the composite control strategy still shows better smoothness and steady-state convergence characteristics.

The error time–domain curve is shown in Figure 9. The error curve of the RBF–PID–admittance hybrid controller is kept within ±2° in the steady-state phase, and it can converge quickly when unloading and positioning in stage IV, and the adjustment time

is obviously shortened. The root-mean-square error index shows that RBF-PID control reduces the RMSE of Bucket, Arm, and Boom joints by 83.9%, 13.2%, and 13.4%, respectively, compared with PID. Among them, the improvement of the Bucket joint is the most obvious, indicating that the online parameter tuning of the neural network effectively compensates for time-varying uncertainty. However, due to the small initial error base of the Arm and Boom joints, the improvement of the adaptive mechanism is relatively limited. After further introducing admittance control, compared with RBF-PID, the RMSE of the RBF–PID–admittance hybrid control strategy is reduced by 33.2%, 25.3%, and 10.2% in the Arm, Boom, and Bucket joints, respectively. The admittance link improves the accuracy of the Arm and Boom joints more obviously, and the force–position hybrid adjustment mechanism can effectively suppress the tracking deviation caused by force impact.

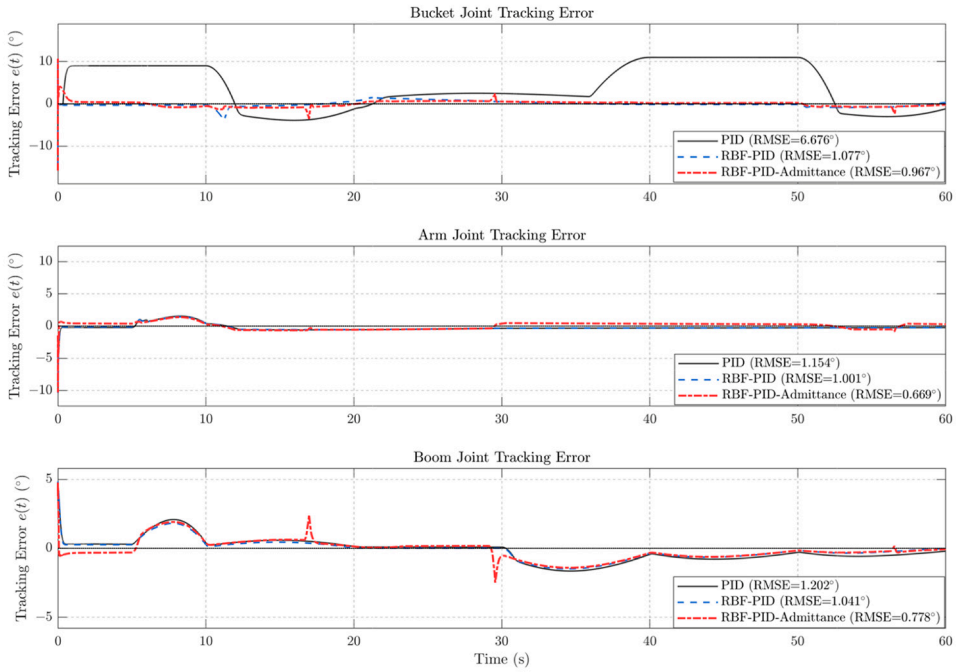


Figure 9. Controller error curve.

The trajectory tracking error statistics are shown in Table 8. Compared with PID control, the RMSE of the RBF–PID–admittance hybrid controller in Bucket, Arm and Boom joints is reduced by 85.5%, 42.0% and 35.3%, respectively, and the average absolute error is reduced by 88.5%, 18.5% and 31.0%. In particular, the incorporation of the admittance control loop further decreases the RMSE of the arm and boom joints by 33.2% and 25.3% relative to the RBF-PID baseline, thereby confirming the effectiveness of the force–position hybrid regulation scheme in suppressing tracking deviations induced by force impacts. Although the MAE of the bucket joint exhibits a slight increase over that of the RBF-PID, its RMSE continues to improve, and the overall tracking accuracy is notably enhanced. Although the three controllers have little difference in the maximum absolute error index, the composite control strategy achieves the best RMSE and MAE indicators, indicating that its average tracking accuracy in the whole operation cycle is significantly improved, and the error energy is greatly attenuated. The maximum error usually occurs in the start-up transient of stage I. At this time, the RBF network has not yet converged, and the admittance loop has not yet established a stable contact force. The initial peak error of the three controllers is limited by the physical saturation and initial conditions of the actuator, rather than the steady-state performance of the control law. The significant difference between RMSE and MAE is mainly reflected in the continuous operation of stage II-V, reflecting the ability of the adaptive mechanism to suppress time-varying load.

The computational complexity of the RBF–PID–admittance compound controller is further assessed by counting floating-point operations (FLOPs) per control cycle. The RBF-PID module accounts for 342 FLOPs, while the admittance control loop introduces an additional 151 FLOPs. When estimated on an embedded platform featuring an ARM Cortex-A72 core, the total execution time is approximately 49 ns—substantially lower than the 10 ms control period of the hydraulic system. Consequently, the admittance loop, incurring only a 30.6% increment in computational cost, enables force–position hybrid control functionality that is inherently absent in the PID or RBF-PID baselines. In summary, the RBF–PID–admittance hybrid control strategy effectively improves the trajectory tracking accuracy and anti-interference ability of the excavator through adaptive parameter tuning and force–position hybrid adjustment.

Table 8. Trajectory tracking error statistics.

Controller	Joint	RMSE (°)	MAE (°)	MaxAE (°)	FLOPs
PID controller	Bucket	6.6761	5.4040	15.7944	30
	Arm	1.1539	0.6019	10.3559	
	Boom	1.2019	0.8286	4.8355	
RBF-PID controller	Bucket	1.0773 (↓83.9%)	0.5760 (↓89.3%)	15.7944	342
	Arm	1.0014 (↓13.2%)	0.5559 (↓7.6%)	10.3579	
	Boom	1.0408 (↓13.4%)	0.6375 (↓23.1%)	4.8356	
RBF–PID–Admittance composite controller	Bucket	**0.9674** (↓**85.5%**)	0.6236 (↓88.5%)	15.7919	493
	Arm	**0.6236** (↓**88.5%**)	**0.4903** (↓**18.5%**)	10.2856	
	Boom	**0.7778** (↓**35.3%**)	**0.5714** (↓**31.0%**)	4.8237	

The time-varying curves of RBF–PID–admittance hybrid controller, RBF-PID controller, and PID controller parameters are shown in Figures 10–12, respectively. The proportional–integral–differential gain of the PID controller remains constant throughout the operation cycle. The time-invariant characteristics of the parameters make it impossible to dynamically adjust according to the disturbance intensity in the load mutation stage, and it is difficult to balance the response speed and steady-state accuracy. The Kp of the RBF-PID-controlled bucket joint climbs from the initial value of 10 to 38 by fast learning, and there is a cliff-like fall during the phase transition. This drastic parameter jump reflects the high-sensitivity response of the neural network in the error space: when the tracking error is large, the gradient descent algorithm drives Kp to increase sharply to accelerate convergence; when the load mutation causes the error gradient to reverse, the parameter update exhibits overshoot characteristics. High-frequency parameter switching will excite unmodeled dynamics and lead to discontinuity of control errors, which may cause pressure pulsation and mechanical tremor in actual hydraulic systems. In contrast, the parameter curves of Arm and Boom joints are relatively stable. The RBF–PID–admittance hybrid controller reconstructs the parameter-tuning strategy through the force–position coupling mechanism. The initial value of the Bucket joint Kp is set to 10, which rises rapidly to about 30 in stage I, and continues to rise to about 45 in stage II with an arm slope. Stage III remains high and stable, and stage IV is slightly raised to about 48. Although the total adjustment range is equivalent to that of RBF-PID, the curve does not have the sharp drop in RBF-PID, and the gain level is related to the operation stage, indicating that the force signal feedforward introduced by the admittance link provides the RBF network with a coherent feature vector about the phase of the external load, so that the parameter update is changed from 'error-gradient' to 'condition-mapping'. The Kp of the Arm joint remains constant from about 28 to 32 at 10 s, and the Boom joint is completely locked from about 35 to 38 within 5 s, showing almost fixed-parameter characteristics. This indicates that the admittance control achieves a monotonous, phase-locked structured gain scheduling

for the main bearing joint through the force–position hybrid control strategy, and 'freezes' unnecessary parameter search for the non-main bearing joint through the force-controlled loop feedforward compensation, which not only ensures the control accuracy of the large inertia joint in a wide operating range, but also avoids the risk of excessive parameterization and parameter drift of the small inertia joint.

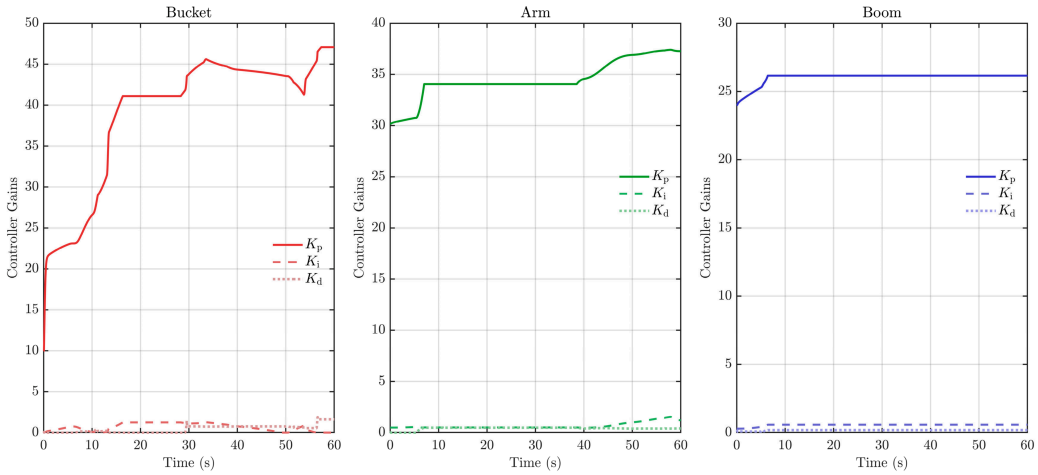


Figure 10. RBF–PID–admittance hybrid controller parameters.

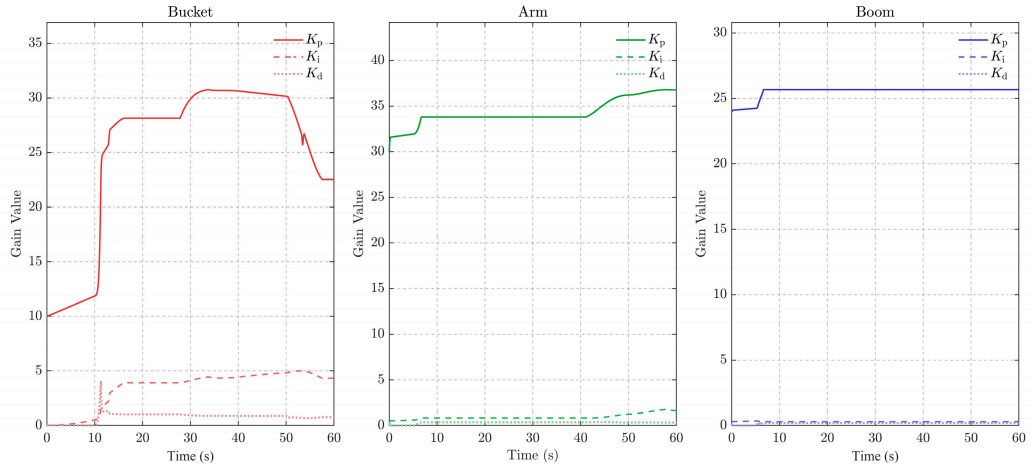


Figure 11. RBF-PID controller parameters.

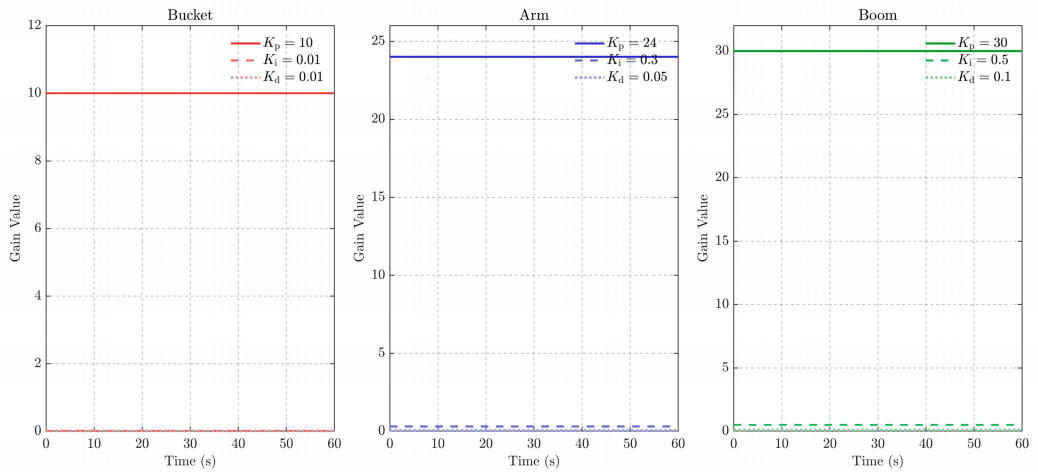


Figure 12. PID controller parameters.

4.3. RBF–PID–Admittance Hybrid Controller Performance Simulation Analysis

In order to verify the performance of the RBF–PID–admittance hybrid control strategy in the excavator working cycle, this paper simulates the typical working cycle simulation scenario (as shown in Figure 13), and sets the 0–60 s digging cycle to investigate the controller's free-space movement, rigid contact, and digging and the adaptive ability of the job. Based on the simulation time series data, the real-time correction characteristics of the reference trajectory by the admittance planning layer, the nonlinear evolution law of the dynamic response of the contact force, and the impedance hysteresis behavior of the force–position coordinated control are analyzed.

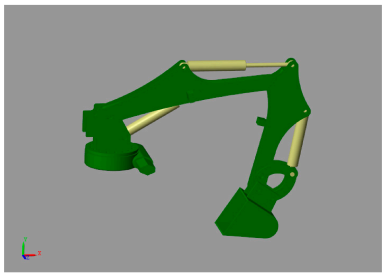


Figure 13. Mining job simulation.

The time–domain response of the admittance trajectory correction of the three joints of Bucket, Arm and Boom is shown in Figure 14. The curve reflects the compensation imposed by the admittance controller on the initial reference trajectory according to the contact force feedback, and the ordinate is the trajectory correction amplitude. In stage I, Bucket makes concessions, and Boom synchronously applies forward bias to optimize the contact configuration. In stage II, the Bucket correction increases to achieve active cut-in, and Arm generates reverse compensation to maintain attitude stability. In stage III, Bucket maintains positive bias to ensure continuous force tracking, Arm maintains negative correction to bear the main reaction force, and Boom provides inertial support. The stability of the curve verifies the suppression of damping on force oscillation. In stage IV, the correction of each joint converges rapidly to positive and negative 1°, and the admittance control exits smoothly. The inverse correction characteristics of Bucket and Arm reflect the coordination mechanism of terminal compliance and attitude stability, which proves the robustness of the admittance planning layer in complex condition switching.

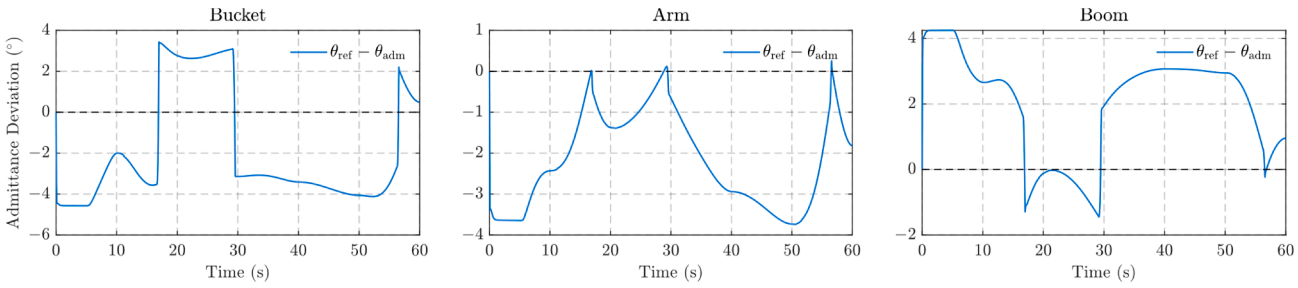


Figure 14. Time–domain response of admittance trajectory correction.

The force tracking performance curve (as shown in Figure 15) reveals the dynamic evolution characteristics of the contact force under the five-stage excavation conditions. In the initial attitude adjustment period of stage I, the bucket moves in free space, and the contact force remains at zero; the system does not interact with the working medium. In the excavation cut-in period of stage II, due to the phase lag coupling between the instantaneous impedance of the soil high-stiffness medium and the inertia term of the admittance controller, the trigger force response is established at about 15 s, and the actual

force rises rapidly and reaches the overshoot peak of 7 × 104 N near 20 s. The subsequent force response attenuation characterizes the rebound characteristics of the soil after elastic unloading, and basically attenuates to zero by 30 s. In the stage III full bucket lifting period, the system is actually in a transition state with load lifting but no significant external contact force. During the unloading positioning of stage IV and the unloading reset of stage V, the contact force is completely zeroed and remains stable, and the bucket has completely separated from the contact surface system and returned to the pure position-control mode. The above time series evolution shows that the admittance force control is only activated in the finite time window of stage II-III, and the force tracking has significant overshoot and undershoot nonlinear characteristics, reflecting the high dynamic complexity of soil–machine interaction.

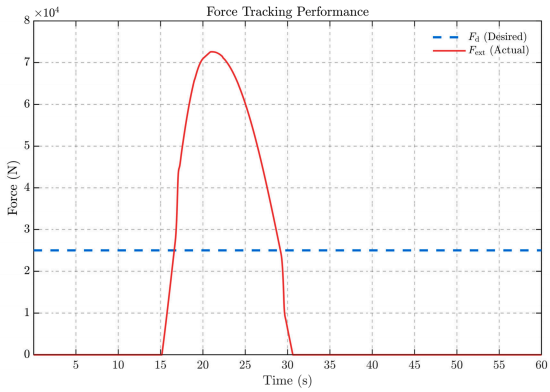


Figure 15. RBF–PID–admittance hybrid controller force tracking performance.

The admittance characteristic phase portrait (as shown in Figure 16) illustrates the phase-space mapping between force error and trajectory correction, along with its temporal evolution. The trajectory morphology reveals the hysteretic nonlinearity and energy dissipation characteristics inherent to the admittance mechanism. In stage I (blue trajectory), the system operates in free-space motion, where both force error and trajectory correction approach zero, with data points densely clustered in the vicinity of the phase-plane origin. During this phase, admittance control remains inactive, implementing only minor pre-contact attitude biases. Upon transitioning to Stages II–III (green, yellow to orange trajectories), the stable engagement phase commences. Following contact establishment, the force error increases abruptly, driving the trajectory correction to transition from negative to positive values. The phase trajectory forms a counter-clockwise hysteresis loop traversing from the third quadrant through the first quadrant. This annular structure characterizes the impedance memory property of the admittance model: the correction response during disengagement lags behind the force error variation during engagement, manifesting the system's dynamic hysteresis effect. The enclosed area of the hysteresis loop quantitatively corresponds to the contact oscillation energy dissipated by the admittance damping term. The geometric asymmetry of the loop indicates the optimized trade-off between penetration efficiency and retraction protection embedded in the control strategy—prioritizing engagement velocity while limiting withdrawal amplitude. In stages IV–V (red trajectory), upon completion of excavation and disengagement from contact, the force error converges to zero, and the phase trajectory returns radially to the coordinate origin. This indicates complete deactivation of admittance control and restoration of pure position-control mode. This phase diagram comprehensively maps the phase transition boundaries and impedance behavior evolution throughout the complete cycle of "free-space–contact–disengagement." The existence of the hysteresis loop demonstrates the robust adaptability of the admittance mechanism to sudden soil stiffness variations, while the return-to-origin characteristic

validates the disturbance-free exit capability of the control strategy during operational mode switching.

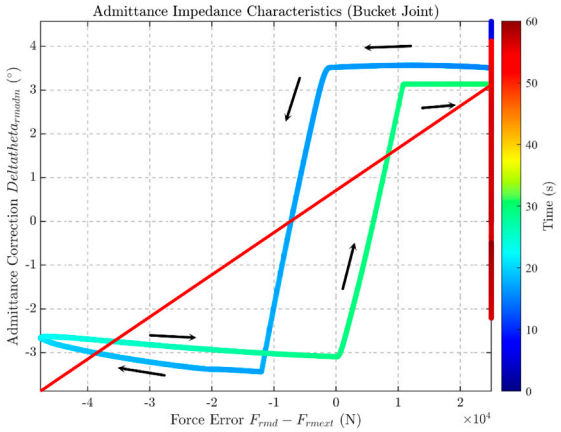


Figure 16. RBF–PID–admittance hybrid controller.

5. Conclusions and Discussion

This study addresses the trajectory tracking and compliance control problems of unmanned excavators operating in soil environments, and proposes an RBF–PID–admittance composite control strategy, which is validated via MATLAB/Simulink simulations. The main conclusions are drawn as follows:

(1) Through the integration of the outer-loop admittance control with the inner-loop RBF neural network, the coordinated optimization of force–position coordination and parameter adaptation is achieved. The admittance loop characterizes the nonlinear soil–tool contact dynamics by exploiting impedance hysteresis properties, thereby realizing compliant contact force responses during the penetration phase and smooth transitions between operational phases. Moreover, the admittance loop feeds forward external load information to the RBF network, shifting the adaptive update mechanism of PID parameters from the conventional "error-gradient" driven paradigm to an "operating-condition-mapping" driven paradigm. This effectively suppresses the gain jump phenomenon commonly encountered in single-network tuning, and enables smooth adjustment of the control gains.

(2) The composite control strategy markedly enhances trajectory tracking performance. In terms of position control, the root-mean-square errors and mean absolute errors for the bucket, boom, and arm joints are all within 1°, while the steady-state errors are maintained within ±2°. Compared with the PID controller, the RBF–PID–admittance composite control reduces the RMSE of the three joints by 85.5%, 42.0%, and 35.3%, respectively, and reduces the MAE by 88.5%, 18.5%, and 31.0%, respectively. Relative to RBF-PID control, the RMSE of the three joints is further reduced from 10.2% to 33.2%.

(3) The stability of the composite control system is established via the Lyapunov method. Under the condition of positive-definite admittance parameters, the admittance loop is input-to-state stable with respect to the torque deviation, and the trajectory deviation is uniformly ultimately bounded, with the convergence region size governed by the upper bound of the torque deviation. The RBF-PID controller equipped with a projection mechanism is semi-globally uniformly ultimately bounded, ensuring that the network weights remain within bounded intervals to prevent parameter drift. Furthermore, by applying cascade system stability theory, it is demonstrated that the overall closed-loop system retains semi-globally uniformly ultimately bounded stability in the presence of bounded external disturbances and neural-network approximation errors.

In the present study, the lumped-parameter approach is employed to simplify the bucket–soil interaction as a mass–spring–damper second-order system. Although this model satisfies the demand for real-time control, its capacity to accurately characterize complex operational scenarios—including soil parameter uncertainty, heterogeneity of compaction, moisture content variations, and diverse excavation materials—remains limited, and its predictive accuracy may be compromised under extreme conditions. The principal limitations of the adopted model are enumerated as follows. (i) The soil elastic modulus E and damping ratio ζ are subject to considerable parametric uncertainties under realistic working conditions. In this work, the admittance parameter M_d^q, C_d^q, K_d^q is selected based on the nominal values of the equivalent mass (combined bucket and soil), the soil damping ratio ζ, and the soil elastic modulus E, respectively. These nominal values are intended to prescribe the desired closed-loop dynamic behavior of the control system. Admittance control does not directly track the aforementioned time-varying parameters; instead, it produces trajectory corrections e_a via the combined effect of torque deviation and sensed soil resistance. Nonetheless, the influence of parametric uncertainty on admittance control performance is not quantitatively assessed. (ii) Spatial heterogeneity in soil compaction induces a non-uniform distribution of bucket cutting resistance along the operational path. The lumped-parameter model, which relies on a single equivalent stiffness to represent the global soil mechanical response, is inherently incapable of capturing local mechanical discontinuities arising from gravel lenses, root systems, or stratified geological formations. (iii) Variations in soil moisture content markedly affect shear strength and stiffness properties—for example, the elastic modulus of saturated soft clay is substantially lower than that of dry sand. However, the fixed-parameter configuration adopted herein does not incorporate moisture content as an explicit variable, thus failing to account for such time-dependent characteristics. (iv) The cutting resistance profiles of different excavation materials differ fundamentally: gravel layers exhibit pronounced discrete impact behaviors, while the temperature-dependent stiffness of frozen soil also lies beyond the descriptive scope of the current linear lumped-parameter model. Should the proposed model be directly applied to non-soil materials, the mapping relationship between torque deviation and trajectory correction would lose its physical foundation.

In the simulation-based validation, the control strategy is evaluated using a simplified hydraulic model. Assumptions including a constant-pressure pump supply, static-gain proportional valve, and neglected leakages may introduce modeling errors under realistic operating conditions. Furthermore, the simulation study has not yet been corroborated by physical experiments; actual control performance is subject to sensor noise, actuator saturation, communication latency, and unmodeled dynamics, which may cause deviations from the simulation outcomes. Subsequent research will focus on developing a refined hydraulic model that accounts for valve dynamics, distributed pipeline parameters, and leakage, alongside sensitivity analyses to quantify the impact boundaries of each simplifying assumption. Concurrently, an online soil parameter identification mechanism will be integrated to maintain real-time computational performance while enhancing adaptability to complex geological settings. Additionally, an experimental platform for autonomous excavation will be constructed to conduct hardware-in-the-loop (HIL) tests and field trials, thereby further validating the proposed method under practical operating conditions.

Author Contributions: Conceptualization, T.W. and X.H.; methodology T.W. and X.H.; software, T.W.; validation, T.W., X.Z. and F.S.; formal analysis, Y.Z.; investigation, X.H. and Y.Z.; resources, X.H.; data curation, T.W., F.S. and X.H.; writing—original draft preparation, T.W. and X.H.; writing—review and editing, T.W., F.S., X.Z., Y.Z. and X.H.; visualization, T.W. and X.H.; supervision, X.Z. and F.S.; project administration, X.H. and F.S.; funding acquisition, X.H. and Y.Z. All authors have read and agreed to the published version of the manuscript.

Funding: This research was funded by the Youth Independent Innovation Fund of Army Engineering University.

Informed Consent Statement: Not applicable.

Data Availability Statement: The simulation code and data that support the findings of this study are available from the corresponding author upon reasonable request.

Acknowledgments: Thanks to all the authors for their participation and efforts in completing this manuscript.

Conflicts of Interest: The authors declare no conflicts of interest.

Appendix A. Dynamics Matrix in Detail

$$\mathbf{M}(\mathbf{q}) = \begin{bmatrix} M_{11} & M_{12} & M_{13} \\ M_{12} & M_{22} & M_{23} \\ M_{13} & M_{23} & M_{33} \end{bmatrix}$$

$$M_{11} = I_{1zz} + I_{2zz} + I_{3zz} + m_1 x_{c1}^2 + m_2(L_1^2 + x_{c2}^2 + 2L_1 x_{c2} c_2) + m_3[L_1^2 + L_2^2 + x_{c3}^2 + 2L_1 L_2 c_2 + 2L_1 x_{c3} c_{23} + 2L_2 x_{c3} c_3]$$

$$M_{12} = I_{2zz} + I_{3zz} + m_2(x_{c2}^2 + L_1 x_{c2} c_2) + m_3[L_2^2 + x_{c3}^2 + L_1 L_2 c_2 + L_1 x_{c3} c_{23} + 2L_2 x_{c3} c_3]$$

$$M_{22} = I_{2zz} + I_{3zz} + m_2 x_{c2}^2 + m_3(L_2^2 + x_{c3}^2 + 2L_2 x_{c3} c_3)$$

$$M_{23} = I_{3zz} + m_3(x_{c3}^2 + L_2 x_{c3} c_3)$$

$$M_{33} = I_{3zz} + m_3 x_{c3}^2$$

$$(\mathbf{J}_{v_1}^{(1)})_z = x_{c1} s_1$$

$$(\mathbf{J}_{v_2}^{(1)})_z = L_1 s_1 + x_{c2} s_{12}$$

$$(\mathbf{J}_{v_2}^{(2)})_z = x_{c2} s_{12}$$

$$(\mathbf{J}_{v_3}^{(1)})_z = L_1 s_1 + L_2 s_{12} + x_{c3} s_{123}$$

$$(\mathbf{J}_{v_3}^{(2)})_z = L_2 s_{123} + x_{c3} s_{123}$$

$$(\mathbf{J}_{v_3}^{(3)})_z = x_{c3} s_{123}$$

$$\mathbf{J}_{\omega_1}^{(1)} = [0, 0, 1]^T$$

$$\mathbf{J}_{\omega 1}^{(1)} = \mathbf{J}_{\omega 2}^{(1)} = \mathbf{J}_{\omega 3}^{(1)} = \mathbf{J}_{\omega 2}^{(2)} = \mathbf{J}_{\omega 3}^{(2)} = \mathbf{J}_{\omega 3}^{(3)}$$

$$\mathbf{C}(\mathbf{q}, \dot{\mathbf{q}}) = \begin{bmatrix} C_{11} & C_{12} & C_{13} \\ C_{21} & C_{22} & C_{23} \\ C_{31} & C_{32} & C_{33} \end{bmatrix}$$

$$C_{11} = [-2m_2 L_1 x_{c2} s_2 - 2m_3(L_1 L_2 s_2 + L_1 x_{c3} s_{23})]\dot{q}_2 + [-2m_3(L_1 x_{c3} s_{23} + L_2 x_{c3} s_3)]\dot{q}_3$$

$$C_{12} = [-m_2 L_1 x_{c2} s_2 - m_3(L_1 L_2 s_2 + L_1 x_{c3} s_{23})](\dot{q}_1 + \dot{q}_2) + [-m_3(L_1 x_{c3} s_{23} + L_2 x_{c3} s_3)]\dot{q}_3$$

$$C_{13} = [-m_3(L_1 x_{c3} s_{23} + L_2 x_{c3} s_3)](\dot{q}_1 + \dot{q}_2 + \dot{q}_3)$$

$$C_{21} = [m_2 L_1 x_{c2} s_2 + m_3(L_1 L_2 s_2 + L_1 x_{c3})]\dot{q}_1 + \left[m_2 L_1 x_{c2} s_2 + m_3(L_1 L_1 L_2 s_2 + L_1 x_{c3} s_{23})]\frac{1}{2}\dot{q}_2 + [m_3 L_1 x_{c3} s_{23}]\frac{1}{2}\dot{q}_2 + [m_3 L_1 x_{c3} s_{23}]\frac{1}{2}\dot{q}_2\right]$$

$$C_{22} = [-m_3 L_2 x_{c3} s_3]\dot{q}_3$$

$$C_{23} = [-m_3 L_2 x_{c3} s_3](\dot{q}_2 + \dot{q}_3)$$

$$C_{31} = [m_3(L_1 x_{c3} s_{23} + L_2 x_{c3} s_3)]\dot{q}_1 + \frac{1}{2}[m_3(L_1 x_{c3} s_{23} + 2L_2 x_{c3} s_3)]\dot{q}_2 + \frac{1}{2}[m_3(L_1 x_{c3} s_{23} + L_2 x_{c3} s_3)]\dot{q}_3$$

$$C_{33} = 0$$

$$\mathbf{G}(q) = \begin{bmatrix} G_1 \\ G_2 \\ G_3 \end{bmatrix}$$

$$G_1 = -g[m_1 x_{c1} s_1 + m_2(L_1 s_1 + x_{c2} s_{12}) + m_3(L_1 s_1 + L_2 s_{12} + x_{c3} s_{123})]$$

$$G_2 = -g[m_2(x_{c2} s_{12}) + m_3(L_2 s_{12} + x_{c3} s_{123})]$$

References

1. Chen, J.; Yang, S.; Kong, X.; Ai, C. High-precision motion control and accurate load estimation of a hydraulic excavator. *Appl. Math. Model.* **2025**, *150*, 116352.
2. Feng, H.; Zhou, H.; Cao, D.; Yin, C.; Zhou, C. Data-driven hydraulic pressure prediction for typical excavators using a new deep learning SCSSA-LSTM method. *Expert Syst. Appl.* **2025**, *275*, 127078. [CrossRef]
3. Rajapakse, R.A. *Construction Engineering Design Calculations and Rules of Thumb*; Butterworth-Heinemann: Oxford, UK, 2016.
4. Zhang, L.; Zhao, J.; Long, P.; Wang, L.; Qian, L.; Lu, F.; Song, X.; Manocha, D. An autonomous excavator system for material loading tasks. *Sci. Robot.* **2021**, *6*, eabc3164. [CrossRef] [PubMed]
5. Zhang, T.; Fu, T.; Ni, T.; Yue, H.; Wang, Y.; Song, X. Data-driven excavation trajectory planning for unmanned mining excavator. *Autom. Constr.* **2024**, *162*, 105395. [CrossRef]
6. Lee, M.; Choi, H.; Kim, C.; Moon, J.; Kim, D.; Lee, D. Precision motion control of robotized industrial hydraulic excavators via data-driven model inversion. *IEEE Robot. Autom. Lett.* **2022**, *7*, 1912–1919. [CrossRef]
7. Shen, Y.; Wang, J.; Feng, C.; Wang, Q. Hybrid-driven autonomous excavator trajectory generation combining empirical driver skills and optimization. *Autom. Constr.* **2024**, *165*, 105523. [CrossRef]
8. Shi, J.; Quan, L.; Zhang, X.; Xiong, X. Electro-hydraulic velocity and position control based on independent metering valve control in mobile construction equipment. *Autom. Constr.* **2018**, *94*, 73–84. [CrossRef]
9. Wang, Z.; Zhou, R.; Hu, C.; Zhu, Y. Online iterative learning compensation method based on model prediction for trajectory tracking control systems. *IEEE Trans. Ind. Inform.* **2022**, *18*, 415–425. [CrossRef]
10. Izadbakhsh, A.; Nikdel, N. Robust adaptive control of cooperative multiple manipulators based on the Stancu–Chlodowsky universal approximator. *Commun. Nonlinear Sci. Numer. Simul.* **2022**, *111*, 106471. [CrossRef]
11. Le Hanh, D.; Ahn, K.K.; Kha, N.B.; Jo, W.K. Trajectory control of electro-hydraulic excavator using fuzzy self tuning algorithm with neural network. *J. Mech. Sci. Technol.* **2009**, *23*, 149–160. [CrossRef]
12. Zhang, Z.; Guo, Y.; Gong, D.; Liu, J. Global integral sliding-mode control with improved nonlinear extended state observer for rotary tracking of a hydraulic roofbolter. *IEEE/ASME Trans. Mechatron.* **2023**, *28*, 483–494. [CrossRef]
13. Liu, L.; Hou, S.; Du, Y.; Li, G.; Wang, Y.; Chen, D.; Zhu, Z.; Song, Z.; Li, X. A trajectory tracking control method for the discharge arm of the self-propelled forage harvester. *Comput. Electron. Agric.* **2024**, *227*, 109627. [CrossRef]
14. Feng, H.; Yin, C.B.; Weng, W.; Ma, W.; Zhou, J.; Jia, W.; Zhang, Z. Robotic excavator trajectory control using an improved GA based PID controller. *Mech. Syst. Signal Process.* **2018**, *105*, 153–168. [CrossRef]
15. Feng, H.; Jiang, J.; Chang, X.; Yin, C.; Cao, D.; Yu, H.; Li, C.; Xie, J. Adaptive sliding mode controller based on fuzzy rules for a typical excavator electro-hydraulic position control system. *Eng. Appl. Artif. Intell.* **2023**, *126*, 107008. [CrossRef]
16. Feng, H.; Song, Q.; Ma, S.; Ma, W.; Yin, C.; Cao, D.; Yu, H. A new adaptive sliding mode controller based on the RBF neural network for an electro-hydraulic servo system. *ISA Trans.* **2022**, *129*, 472–484. [CrossRef] [PubMed]
17. Du, Z.; Ye, Z.; Zhang, H.; Bai, H.; Xu, Y.; Jiang, X. The study of trajectory automatic control based on RBF neural network PID control. In *2015 International Conference on Fluid Power and Mechatronics (FPM)*; IEEE: Piscataway, NJ, USA, 2015; pp. 1169–1173.
18. Choi, J. Development of time varying sliding mode controller with fuzzy system for automatic excavator. In Proceedings of the 28th International Symposium on Automation and Robotics in Construction (ISARC 2011), Seoul, Republic of Korea, 29 June–2 July 2011.
19. Tafazoli, S.; Salcudean, S.E.; Hashtrudi-Zaad, K.; Lawrence, P.D. Impedance control of a teleoperated excavator. *IEEE Trans. Control Syst. Technol.* **2002**, *10*, 355–367. [CrossRef]
20. Qin, T.; Li, Y.; Quan, L.; Yang, L. An adaptive robust impedance control considering energy-saving of hydraulic excavator boom and stick systems. *IEEE/ASME Trans. Mechatron.* **2022**, *27*, 1928–1936. [CrossRef]
21. Dobson, A.A.; Marshall, J.A.; Larsson, J. Admittance control for robotic loading: Design and experiments with a 1-tonne loader and a 14-tonne load-haul-dump machine. *J. Field Robot.* **2017**, *34*, 123–150.
22. Liu, X.; Jiang, H.; Luo, L. Research on Intelligent Control Learning Algorithm in Electrical Engineering Automation Based on Fuzzy Neural Network. *Teh. Vjesn.* **2025**, *32*, 1272–1282. [CrossRef]

23. Chen, H.; Liu, W. Global Residue Harmonic Balance Method for a System of Strongly Nonlinear Oscillator. *Math. Probl. Eng.* **2021**, *2021*, 6641742. [CrossRef]
24. Zhu, R.; Li, W.; Boukerche, A.; Yang, Q. Energy-aware DRL-based dual-perception fountain codes for resource-constrained UASNs. *IEEE Trans. Sustain. Comput.* **2026**, *11*, 111–122. [CrossRef]
25. Wang, H.; Zhao, L.; Peng, Q. An improved sand cat swarm optimization algorithm and its application to agricultural robot path planning. *Eng. Comput.* **2025**, *42*, 1525–1553. [CrossRef]
26. Wang, E.; Xia, J.; Li, J.; Sun, X.; Li, H. Parameters exploration of SOFC for dynamic simulation using adaptive chaotic grey wolf optimization algorithm. *Energy* **2022**, *261*, 125146. [CrossRef]
27. Li, S.; Zhou, G.; Wang, S.; Jia, X.; Hou, L. Multi-sensor data fusion and deep learning-based prediction of excavator bucket fill rates. *Autom. Constr.* **2025**, *171*, 106008. [CrossRef]
28. Ding, H.; Sang, Z.; Li, Z.; Shi, J.; Wang, Y.; Meng, D. Trajectory planning and control of large robotic excavators based on inclination-displacement mapping. *Autom. Constr.* **2024**, *158*, 105209. [CrossRef]
29. Mitrev, R.; Janošević, D.; Marinković, D. Dynamical modelling of hydraulic excavator considered as a multibody system. *Tech. Gaz./Teh. Vjesn.* **2017**, *24*, 327. [CrossRef]
30. Gong, J.; Chen, J.; Cai, D.; Wei, W.; Long, Y. Disturbance observer-based passivity and impedance control for trajectory tracking in autonomous hydraulic excavators. *Autom. Constr.* **2025**, *170*, 105898. [CrossRef]
31. Wang, L.; Chai, T.; Zhai, L. Neural-network-based terminal sliding-mode control of robotic manipulators including actuator dynamics. *IEEE Trans. Ind. Electron.* **2009**, *56*, 3296–3304. [CrossRef]
32. Yao, Z.; Zhang, W.; Lin, C.; Lin, T. Trajectory tracking control of intelligent excavator employing an improved ABSMC based on parameter hierarchical. *Res. Sq.* **2025**. [CrossRef] [PubMed]
33. Feng, H.; Qiao, W.; Yin, C.; Yu, H.; Cao, D. Identification and compensation of non-linear friction for a electro-hydraulic system. *Mech. Mach. Theory* **2019**, *141*, 1–13. [CrossRef]
34. Feng, H.; Zhong, Y.; Zhou, C.; Ji, S.; Yin, C.; Cao, D. Collaborative high-precision trajectory control for heavy excavators based on an improved particle swarm optimization algorithm. *Autom. Constr.* **2025**, *180*, 106546. [CrossRef]
35. Sotiropoulos, F.E.; Asada, H.H. A model-free extremum-seeking approach to autonomous excavator control based on output power maximization. *IEEE Robot. Autom. Lett.* **2019**, *4*, 1005–1012. [CrossRef]
36. Wagner, W.J.; Soylemezoglu, A.; Driggs-Campbell, K. In-Situ Soil-Property Estimation and Bayesian Mapping with a Simulated Compact Track Loader. *arXiv* **2025**, arXiv:250722356.
37. Mohammadi, M.; Karparvarfard, S.H.; Razavizadeh, N.; Tekeste, M.; Moazeni_kalat, A.; Nematollahi, M.A.; Namjoo, M.; Rostami, M.A. Simulation of interaction between soil and rotary tiller to predict the power consumption and investigation of surface soil mixing. *Soil Tillage Res.* **2025**, *252*, 106626. [CrossRef]
38. Zhao, P.; Gao, X.; Ju, X.; Yang, P.; Song, Q.; Huang, Y.; Zheng, Z. Optimization of the front-mounted fertilizer pipe strip rotary tillage device by modeling the wide-seedbed characteristics and power consumption. *Comput. Electron. Agric.* **2024**, *227*, 109624. [CrossRef]
39. Sang, Q.; Xiong, Y.; Zheng, R.; Bao, X.; Ye, G.; Zhang, F. A hybrid contact approach for modeling soil-structure interaction using the material point method. *J. Rock Mech. Geotech. Eng.* **2024**, *16*, 1864–1882. [CrossRef]
40. Behera, A.; Raheman, H.; Thomas, E. A comparative study on tillage performance of rota-cultivator (a passive–active combination tillage implement) with rotavator (an active tillage implement). *Soil Tillage Res.* **2021**, *207*, 104861. [CrossRef]
41. Okada, T.; Yamamoto, T.; Doi, T.; Koiwai, K.; Yamashita, K. Database-driven model predictive control system for online adaptation of an autonomous excavator to environmental conditions. *Control Eng. Pract.* **2024**, *145*, 105843. [CrossRef]
42. Franceschini, N.; Thangeda, P.; Ornik, M.; Hauser, K. Autonomous Excavation of Challenging Terrain using Oscillatory Primitives and Adaptive Impedance Control. In *Proceedings of the 2025 IEEE International Conference on Robotics and Automation (ICRA)*; IEEE: Piscataway, NJ, USA, 2025.
43. Sotiropoulos, F.E.; Asada, H.H. Dynamic modeling of bucket-soil interactions using Koopman-DFL lifting linearization for model predictive contouring control of autonomous excavators. *IEEE Robot. Autom. Lett.* **2021**, *7*, 151–158. [CrossRef]
44. AL-Assady, A.A.M.H.; AL-Khafaji, M.T.J. Design and analysis of electro-hydraulic servo system for speed control of hydraulic motor. *J. Eng.* **2013**, *19*, 562–573.
45. Khedr, O.H.; Awad, M.I.; Al-Oufy, A.K.; Maged, S.A. Optimizing power consumption and position control in an electro-hydraulic system with cylinder bypass and NN-MPC. *Sci. Rep.* **2024**, *14*, 1993. [CrossRef] [PubMed]

Disclaimer/Publisher's Note: The statements, opinions and data contained in all publications are solely those of the individual author(s) and contributor(s) and not of MDPI and/or the editor(s). MDPI and/or the editor(s) disclaim responsibility for any injury to people or property resulting from any ideas, methods, instructions or products referred to in the content.